The structure of the Temsamane fold-and-thrust stack (eastern Rif, Morocco): Evolution of a transpressional orogenic wedge

CrossMark

Antonio Jabaloy-Sánchez [a,*], Ali Azdimousa [b], Guillermo Booth-Rea [a,c], Lahcen Asebriy [d], Mercedes Vázquez-Vílchez [e,f], José Miguel Martínez-Martínez [a,c], Janet Gabites [g]

[a] Univ. Granada, Geodinámica, Granada, Spain
[b] Laboratoire LGA, Faculté des Sciences, Université Mohammed I, Oujda, Morocco
[c] Instituto Andaluz de Ciencias de la Tierra UGR-CSIC, Avda. de las Palmeras, 18100 Armilla, Granada, Spain
[d] Institut Scientifique, B.P. 703, Université Mohammed V, Agdal-Rabat, Morocco
[e] Andean Geothermal Center of Excellence (CEGA), Universidad de Chile, Santiago, Chile
[f] Department of Geology, Universidad de Chile, Santiago, Chile
[g] Pacific Centre for Isotope and Geochemical Research, Department of Earth and Ocean Sciences, The University of British Columbia, 6339 Stores Road, Vancouver, BC V6T 1Z4, Canada

ARTICLE INFO

ABSTRACT

The structure of the Temsamane fold-and-thrust stack corresponds to four units limited by anastomosing ductile shear zones cutting a trend of south verging recumbent folds. This ductile stack was formed in an inclined left-handed transpressional zone at the North African paleomargin during Chattian to Langhian times producing two main deformational events. The first event (D_p) produced a S_p/L_p planar linear fabric generated in a non-coaxial deformation with a top-to-the-WSW sense of movement and was associated to metamorphic P–T conditions varying from late diagenesis in the southernmost Temsamane outcrops to epizone in the north. According to the $^{40}Ar/^{39}Ar$ ages, this deformation occurred at Chattian–Aquitanian times. The second deformational event (D_c event) generated ENE–WSW trending folds with SSE vergence and a set of anastomosing shear zones with S_m/L_m planar linear fabric. The latter units were generated at around 15 Ma (Langhian), and indicate a strong localization of the simple shear component of the transpression. Moreover, this orientation is compatible with the kinematics of the Temsamane detachment, which can explain most of the uplift of the Temsamane rocks from the middle to the uppermost crust. The described evolution indicates that collision between the western Mediterranean terranes and the North African paleomargin and the formation of the Rifean orogenic wedge occurred at Chattian to Langhian times.

1. Introduction

The original concept of transpression/transtension was defined by Harland (1971) and Sanderson and Marchini (1984) as strike–slip deformations that deviate from simple shear because of a shortening (or extension) component orthogonal to the deformation zone. As most plate tectonic kinematics are oblique to plate boundaries, transpression/transtension is one of the most common deformational regimes in the lithosphere (Dewey et al., 1998). Different theoretical models have been proposed to determine a mathematical description of transpressional zones and the evolution of their fabrics and structures (e.g., Dewey et al., 1998; Jiang et al., 2001; Czeck and Hudleston, 2003; Fernández and Díaz-Azpiroz, 2009; among others). The primary

difficulty is the complex and poorly understood deformation patterns that were generated in many transpression zones, where field studies show that structures differing significantly in orientation may form simultaneously (e.g., Dewey et al., 1998).

The theoretical models pose several questions related with the deformation of the transpressional zones. One of these questions is whether the strain is non-partitioned or partitioned in the deformation zone (Dewey et al., 1998). Most of the models on transpressional deformation zones assume that the strain must be partitioned into the boundary-normal strain and the boundary-parallel strain components (e.g., Dewey et al., 1998; Jiang et al., 2001; Molnar, 1992; Platt, 1993). Moreover, most of the models assume a deformational zone with vertical geometry, whereas dipping deformational zones or the so-called inclined transpressional zones are scarcely discussed (Dutton, 1997; Jones et al., 2004).

Furthermore, most of the transpressional zones suggest localization of the non-coaxial component of the transpression (simple shear),

* Corresponding author. Tel.:+34 958 243365; fax: 34 958 248527.
  E-mail address: jabaloy@ugr.es (A. Jabaloy-Sánchez).

whereas the coaxial component remains non-localized in the entire deformational zone (Jiang et al., 2001; Lin et al., 1998).

Another major question is the presence of differential vertical movements within the parts of the transpressional wedge, producing the exhumation of rocks from deep crustal levels (e.g., Spotila et al., 2007).

The eastern Rif forms the southern branch of the Betic–Rif orogen (Fig. 1), and is considered an orogenic belt formed in a left-lateral transpressive regime (e.g., Platt et al., 2003, 2013; Booth-Rea et al., 2005; Balanyá et al., 2007). It is essentially composed of Mesozoic to Cenozoic rocks affected by ductile penetrative deformations and low- and very low-grade metamorphism that decreases westwards (Frizon de Lamotte, 1985, 1987; Negro et al., 2007; Suter, 1980), suggesting that most eastern Rif rocks were buried at depth during the Alpine orogeny and later exhumed to the surface. The mode and age of deformation and exhumation of these metamorphic rocks in the inclined transpressional zone is not well known; only recently Booth-Rea et al. (2012) have proposed a mechanism for the exhumation of part of the eastern Rif's lowermost units (Temsamane fold-and-thrust stack) by means of a brittle–ductile extensional detachment.

The main aim of this work is to analyze the structure of the Temsamane fold-and-thrust stack in the eastern Rif in order to establish its tectono-metamorphic evolution. To do so, we present new structural, metamorphic and radiometric ages that constrain the evolution and exhumation mechanisms for the regional metamorphic rocks. The understanding of how and when these metamorphic rocks were deformed and exhumed constitutes a key to the evolution of the Betic–Rif orogen and the western Mediterranean area as well as for other transpressive orogenic belts. The main reason is that it can improve our knowledge of the vertical movements of rocks within a transpressional deformation zone and its relationship with both the strain partitioning and localization of the strain components in an inclined transpressional zone.

2. Geological setting

The Rif is an Alpine mountain belt fringing northern Morocco that continues towards the Betic belt in southern Spain to form the Betic–Rif orogen (e.g., Booth-Rea et al., 2005; Chalouan et al., 2008; Platt et al., 2013 and references therein). This orogen resulted from the westward movement of the Alborán domain (Balanyá and García-Dueñas, 1987), at the same time as the African and Eurasian plates converged (e.g., Chalouan and Michard, 2004; Jolivet et al., 2003) (Fig. 1). During the movement of the Alborán domain, both the South Iberian and the North African paleomargins were subducted, producing HP metamorphism in the rocks of the South Iberian margin, namely the Nevado–Filábride complex in the Betic orogen (Behr and Platt, 2012; Gómez-Pugnaire et al., 2012), and IP–LT metamorphism in the rocks of the north African paleomargin (Negro et al., 2007, 2008).

The Rif is composed of three main structural domains from the south towards the Mediterranean coast: the External Rif, the Maghrebian Flyschs nappe complex, and the Internal Rif or Alborán domain (Fig. 1). The External Rif is mainly formed of Mesozoic to Cenozoic sediments and metasediments, and is interpreted as the North African passive margin of the Tethys Ocean, although recently, part of the External Rif (Mesorif) has been interpreted as rest of ophiolitic units that may represent allochthonous remnants of the Tethyan oceanic floor (Benzaggagh et al., 2014). Their rocks are overthrust by the Maghrebian Flyschs units. The rocks of the Maghrebian Flyschs nappe complex are mainly turbidites and also include basalts with MORB affinities interpreted as rocks from the main suture of the Tethys Ocean (Duran-Delga et al., 2000). They are overthrust by the Internal Rif or Alborán domain. The deformations affecting the North African paleomargin ranged mainly from the Oligocene to the Miocene (Chalouan and Michard, 2004; Chalouan et al., 2008).
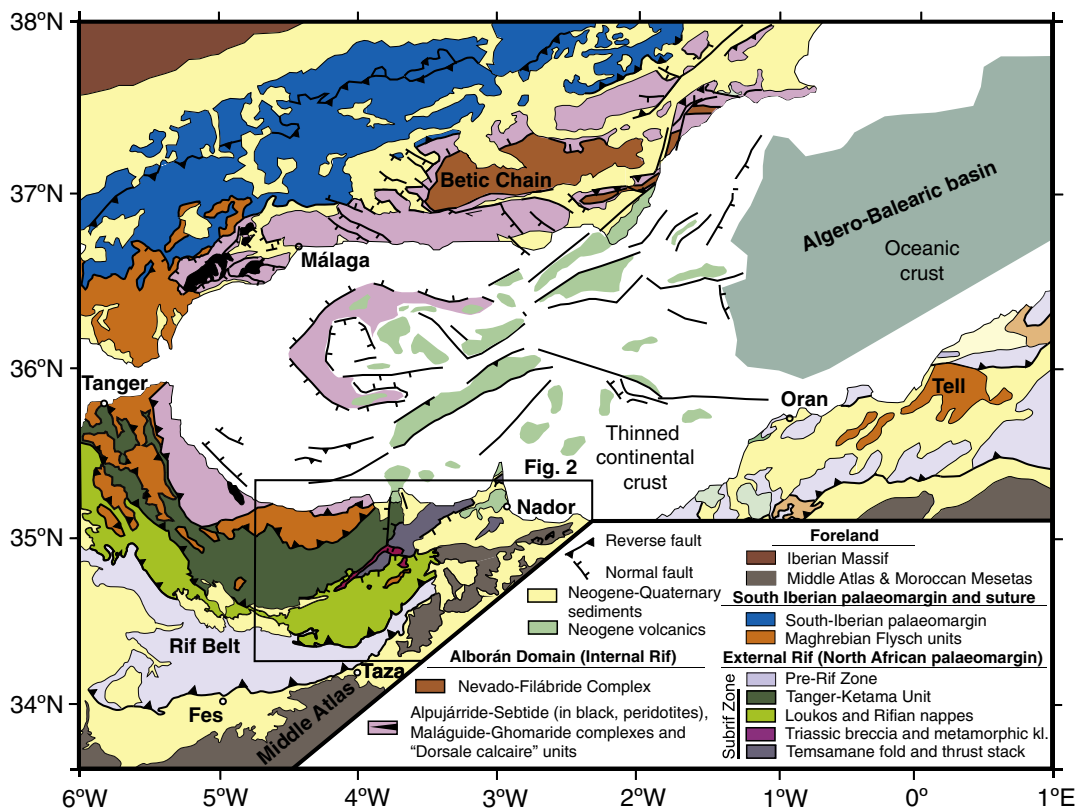

Fig. 1. Geological map of the main geological domains in the Betic–Rif orogenic system surrounding the Alborán Sea. The location of the study area represented in Fig. 2 is marked with the black rectangle.

The External Rif can be grouped into two main zones: the Prerif and the Subrif (Asebriy et al., 1987) (Figs. 1 and 2). The Prerif zone, south of the Rif belt, is a sedimentary complex of olistostromes with Paleozoic to Cenozoic blocks in a matrix of mainly Tortonian marls (Bourgois, 1977; Leblanc, 1975–1979; Suter, 1980; Vidal, 1971). The Subrif zone (Asebriy et al., 1987) includes the Intrarif and Mesorif units as defined by Durand-Delga et al. (1962). It is composed of diagenetic to low-grade metamorphic rocks deformed under brittle to ductile conditions (Andrieux, 1971; Asebriy, 1994; Asebriy et al., 2003; Azdimousa et al., 1998, 2007; Frizon de Lamotte, 1985; Michard et al., 1992). The stratigraphic sequences of the Subrif zone are characterized by a continuous Lower Jurassic to Cretaceous mostly pelitic succession. As previously mentioned, several of the Subrif lithological sequences (Mesorif) cover mafic and ultramafic massifs with ophiolitic affinities that can be alternatively envisaged as rests of an intramargin suture zone or parts of the Tethyan oceanic seafloor (Benzaggagh et al., 2014).

In the Eastern Rif (Fig. 2), the Subrif zone includes three main sets of tectonic units that are, from bottom to top: the Temsamane fold-and-thrust stack, the Tanger-Ketama unit, and the Aknoul units. The latter units continue towards the western Rif, where they are known as the Aknoul and Loukos units (Fig. 1).

The Temsamane fold-and-thrust stack includes the lowest tectonic units of the Subrif zone and their lithological sequence begins with dark Paleozoic schists covered by Jurassic marbles. Continuing up section, whitish Berriasian–Barremian phyllites and shales alternate with marbles, and are covered by dark Aptian–Early Albian phyllites and shales alternating with quartzites (Fig. 3) (Azdimousa et al., 2007). Several metabasite bodies metamorphosed under Green Schists facies are located at the transition between the dark Paleozoic schists and the Jurassic marbles, while small serpentinite bodies crop out on the thrust surfaces (Fig. 3) (Azdimousa et al., 2007). Negro (2005) and Negro et al. (2007) estimated the metamorphic conditions of the rocks of the uppermost Temsamane unit (Ras Afraou unit) at 350 ± 30 °C and 7–8 kbars. The lower Temsamane units crop out in the south part of the belt and underwent lower pressures and temperatures (Negro, 2005; Negro et al., 2007). $^{40}Ar/^{39}Ar$ radiometric ages on white micas range between 23 and 8 Ma (Monie et al., 1984; Negro et al., 2008). Negro et al. (2008) interpret the older Oligocene ages as being the age of the metamorphism, and the Middle and Late Miocene ages as being the exhumation age of the rocks.

The rocks of the Temsamane fold-and-thrust stack are affected by strong planar–linear fabrics with an ENE–WSW trending stretching
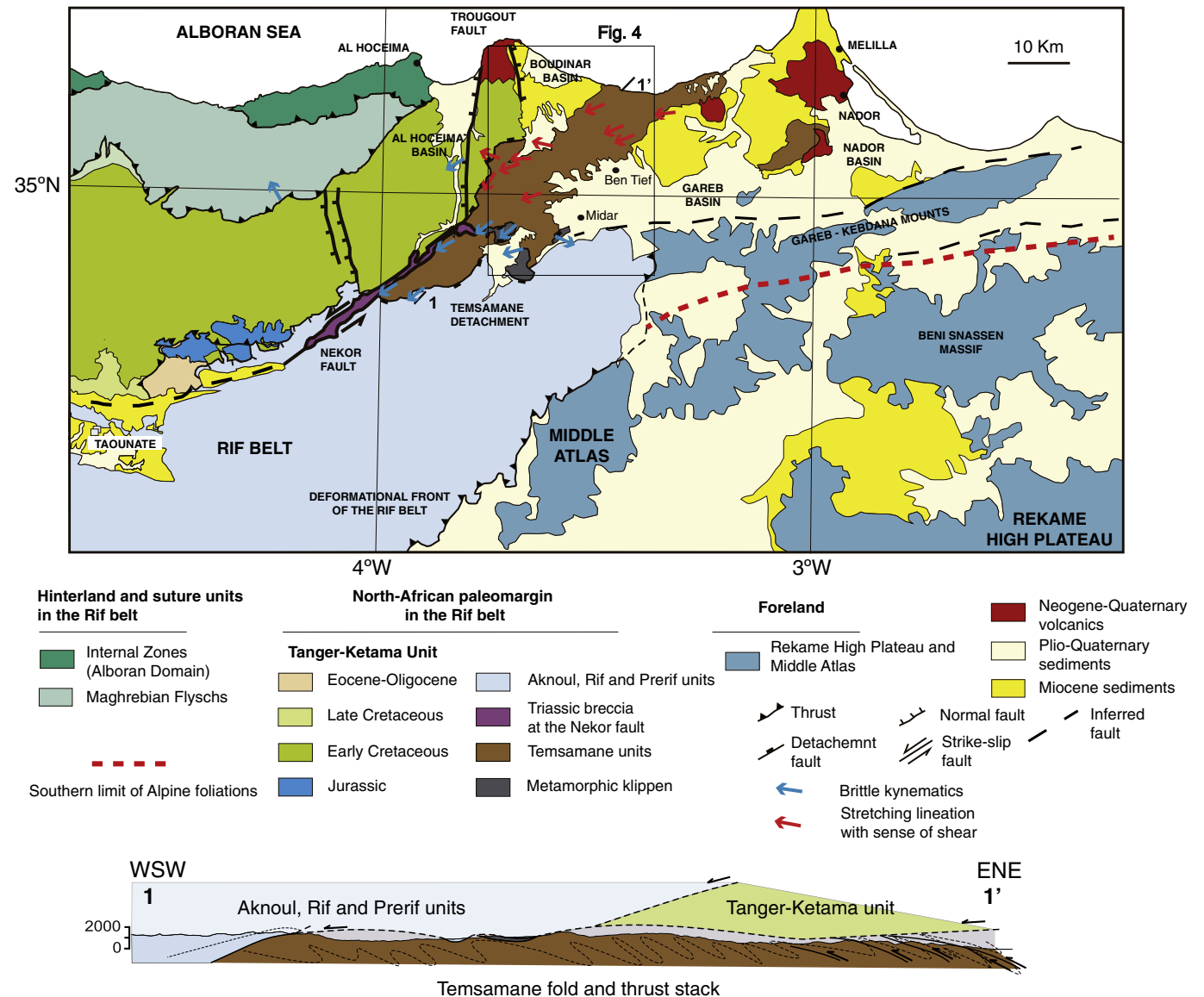

Fig. 2. Geological map of the Eastern Rif area modified from Suter (1980). We have added the different types of tectonic contacts in the area, their tectonic transport, and the southern front of development of the Alpine foliation. Below is the geological cross-section 1-1′, showing the geometry of the detachment and its union with the normal fault at the top of the Tanger–Ketama unit.

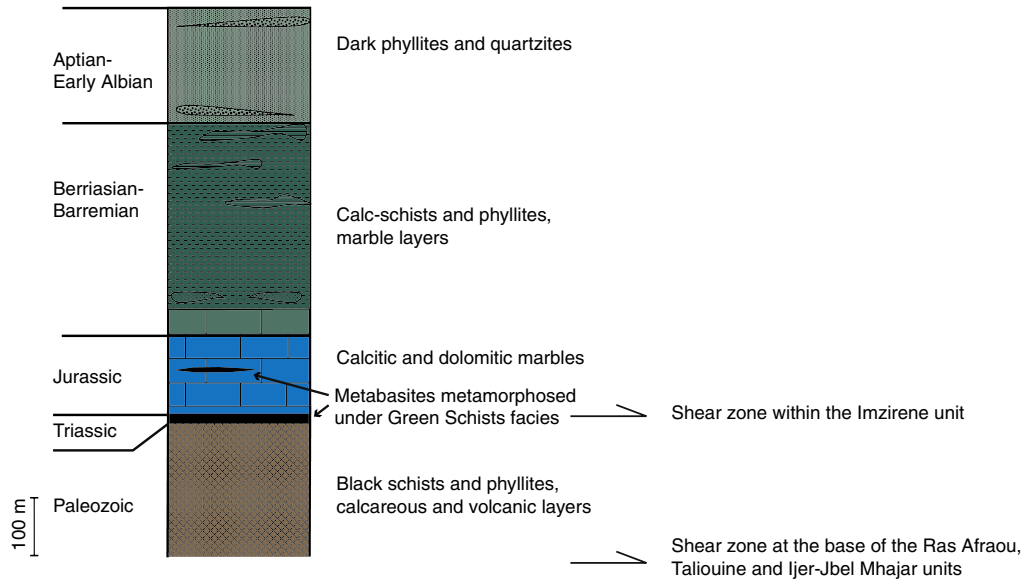# Lithological sequence of the Temsamane fold and thrust stack

Fig. 3. Lithological sequence of the Temsamane fold-and-thrust stack (Eastern Rif area).

lineation (Frizon de Lamotte, 1985, 1987). The kinematic criteria indicate that this fabric formed with a top-to-the-WSW sense of shear (Frizon de Lamotte, 1985, 1987). Recently, Azdimousa et al. (2007) and Booth-Rea et al. (2012) described regional-scale recumbent folds with ENE–WSW trending hinges and SSE vergence cut by ductile shear zones and thrusts.

The Tanger–Ketama unit overthrusts the Temsamane fold-and-thrust stack (Figs. 1 and 2). Its lithology is a sequence of Early Jurassic to Latest Albian carbonates and metapelites affected by extensional metamorphism with late diagenesis to anchizone conditions (Leikine et al., 1991; Vázquez et al., 2013, in press). The K/Ar radiometric ages on white micas range from 131.9 ± 3.2 Ma to 78.0 ± 1.2 Ma, indicating a Cretaceous age for the extensional metamorphic event (Azdimousa et al., 1998, 2003); apatite fission-track ages show that the rocks cooled below 120 °C between 17 and 13 Ma (Azdimousa et al., 1998, 2003). The Beni-Malek ultramafic body (composed of partially serpentinized spinel lherzolites) is located at the base of this unit (Elazzab et al., 1997; Michard et al., 1992, 2007). The rocks of the Tanger–Ketama unit are affected by a slaty cleavage parallel to the lithological layering (S_1). This S_1 slaty cleavage forms the main reference surface in the Tanger–Ketama sequence and is affected by southward-vergent recumbent folds with associated crenulation cleavage (S_2) (Vázquez et al., 2013, in press).

The Aknoul units are composed of Upper Cretaceous to Lower Miocene rocks, and they are interpreted as the upper part of the Tanger–Ketama sequence, which were detached and thrust over the foreland rocks of the Middle Atlas (e.g., Chalouan et al., 2008). Exhumation of the Temsamane metamorphic rocks took place along a major extensional detachment with movement towards the WSW: the Temsamane detachment system that separates the Temsamane fold-and-thrust stack in the footwall from the Tanger–Ketama and Aknoul units in the hanging wall (Booth-Rea et al., 2012).

3. Methodology

3.1. X-ray diffraction (XRD)

The fine-grained metapelites from the Temsamane fold-and-thrust stack were studied by X-ray diffraction (XRD) to determine mineral assemblages and metamorphic conditions. Thirty-seven unaltered shale, slate, and phyllites samples (Fig. 4, Table 1) were carefully collected

and washed; after coarse crushing, homogeneous rock chips were used for XRD preparation. Whole-rock samples and the clay fraction (<2 μm) were studied using a Philips PW 1710 X-ray diffractometer with Cu-Kα radiation, graphite monochromator, and automatic divergence slit (Department of Mineralogy and Petrology, University of Granada, Spain).

The <2 μm fractions were separated by repeated extraction of supernatant liquid subsequent to settling. Orientated aggregates were prepared by sedimentation on glass slides. Preparation of samples and experimental conditions for illite crystallinity measurements (Kübler Index, KI) were carried out according to IGCP 294 IC Working Group recommendations (Kisch, 1991). Our KI measurements (y) were transformed into C.I.S. values (x) according to the equation $y = 1.6583x - 0.0484$ ($r = 0.9996$), obtained in the Granada Laboratory using the inter-laboratory standards of Warr and Rice (1994). The KI values were measured for the <2 μm fractions and for the bulk-rock samples. The b-cell parameters of micas and chlorites were obtained from the 060 peaks measured on rock slices cut normal to the sample foliation. For all spacing measurements, quartz from the sample itself was used as the internal standard.

3.2. $^{40}Ar/^{39}Ar$ methodology

The samples for $^{40}Ar/^{39}Ar$ determinations (Fig. 4, Table 2) were crushed in a ring mill, washed in distilled water and ethanol, and sieved when dry to collect the 0.25–0.38 mm fraction. Appropriate mineral grains were hand-picked under a microscope out of the bulk fraction. These mineral separates were wrapped in aluminum foil and stacked in an irradiation capsule with similar-aged samples and neutron flux monitors (Fish Canyon Tuff sanidine: FCs, 28.03 Ma; Renne et al., 1998).

The samples were irradiated on May 2 and 4 of 2011 at the McMaster Nuclear Reactor in Hamilton, Ontario, at 90 MWH, with a neutron flux of approximately 6×10^{13} neutrons/cm^2/s. Analyses (n = 36) of 12 neutron flux monitor positions produced errors of <0.5% in the J value.

The samples were analyzed from May to October of 2011 at the Noble Gas Laboratory (Pacific Centre for Isotopic and Geochemical Research, University of British Columbia). The mineral separates were step-heated at incrementally higher powers in the defocused beam of a 10 W CO_2 laser (New Wave Research MIR10) until fused. The gas evolved from each step was analyzed by a VG5400 mass spectrometer
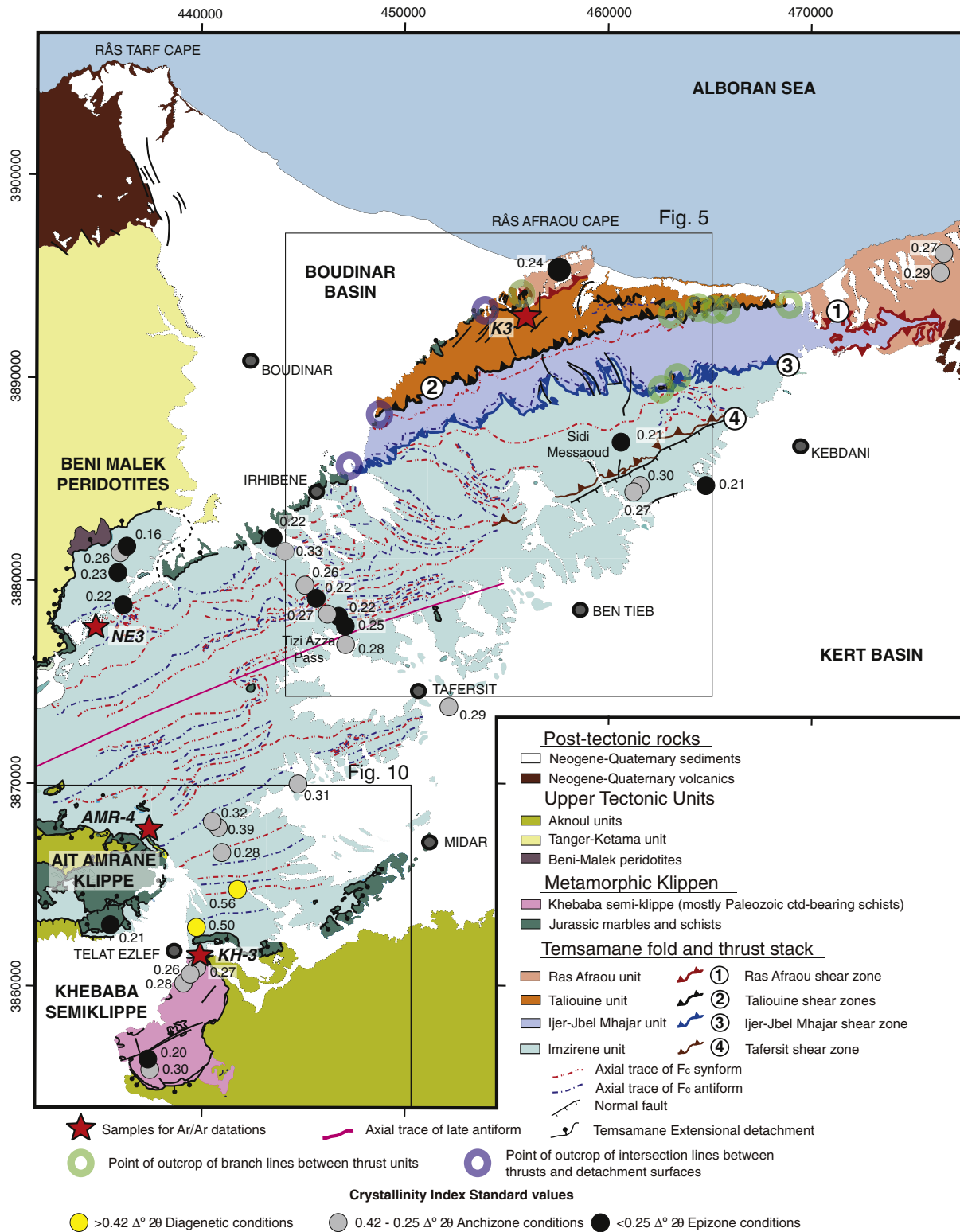
Fig. 4. Sketch of the main geological units in the central part of the outcrops of the Temsamane fold-and-thrust stack. See Fig. 2 for location. We have added the axial traces of the F$_c$ folds in the Temsamane fold-and-thrust stack and the location of samples for XRD analyses (circles; Table 1), for microbeam analyses, and for ^{40}Ar/^{39}Ar determinations (stars, Table 2).

equipped with an ion-counting electron multiplier. All measurements were corrected for total system blank, mass spectrometer sensitivity, mass discrimination, radioactive decay during and subsequent to irradiation, as well as interfering Ar from atmospheric contamination and the irradiation of Ca, Cl and K (isotope production ratios: (^{40}Ar/^{39}Ar)$_K$ = 0.0302 ± 0.00006, (^{37}Ar/^{39}Ar)$_{Ca}$ = 1416.4 ± 0.5, (^{36}Ar/^{39}Ar)$_{Ca}$ = 0.3952 ± 0.0004, Ca/K = 1.83 ± 0.01(^{37}Ar$_{Ca}$/^{39}Ar$_K$)).

4. Structure of the Temsamane fold-and-thrust stack

The main outcrop of the Temsamane fold-and-thrust stack forms a NE–SW trending mountain range that can reach elevations of over 1400 m. It is bounded to the northwest by the triangular Late Tortonian to Quaternary Boudinar sedimentary basin (Azdimousa et al., 2006) and to the south by the plains of the Neogene Kert basin (Fig. 4). Middle to

Table 1
Crystal-chemical parameters and bulk mineralogy of Temsamane units.

				White mica					Chlorite				
				d_{001} Å		b Å	Illite "Crystalinity" (KI) "CIS" scale Δ° 2Θ		d_{001} Å		b Å	Mineral composition Qtz and Ms (all samples)	
Samples	X	Y	Age	<2 μm	Total		<2 μm	Total	<2 μm	Total			Unit
KET-11	426763	3863855	Berri.-Barrem.	10.001	9.988	9.01	0.22	0.23	14.15	14.14	9.253	Cal. Chl	Temsamane
KET-12*	461076	3884185	Berri.-Barrem.	9.999	9.999	–	0.3	0.25	14.13	14.13	9.251	Cal. Chl. Pg	Temsamane
KET-13*	461036	3884435	Berri.-Barrem.	9.999	10.005	–	0.27	0.16	14.14	14.14	9.251	Cal. Chl. Pg	Temsamane
KET-14*	460445	3886670	Aptian-Albian	9.965	9.974	9.002	0.21	0.22	–		9.24	Pg. Kln	Temsamane
KET-15	457169	3894899	Paleozoic	9.98	9.969	9.007	0.24	0.22	–	14.12	9.258	Kln	Temsamane
KET-16	481170	3897781	Paleozoic	9.976	9.976	–	0.27	0.24	–	14.12	–	Kln	Temsamane
KET-17*	479018	3897477	Paleozoic	9.974	9.969	–	0.29	0.21	–	–	–	Kln. Chl. Pg	Temsamane
TSM-1*	439321	3854362	Triassic	9.996	9.994	8.997	0.3	0.28	–	–	9.261	Kln. Pg	Temsamane
TSM-2	464834	3884536	Triassic	9.957	9.953	–	0.21	0.15	14.14	14.15	9.258	Chl. Plg	Temsamane
RAS-1*	459104	3895452	Paleozoic	9.971	9.967	9.007	0.25	0.2	14.13	14.13	9.253	Chl. Pg	Temsamane
RAS-2*	459104	3895452	Paleozoic	9.976	9.967	–	–	0.18	14.13	14.16	–	Cal. Chl. Pg	Temsamane
BMK-1	436094	3878806	Berri.-Barrem.	9.978	9.971	9.02	0.22	0.13	14.15	14.15	9.256	Pl. Chl	Temsamane
BMK-2*	435854	3880518	Aptian-Albian	9.98	10.005	–	0.24	0.21	14.12	14.14	9.257	Pl. Chl. Pg	Temsamane
BMK-3	435893	3880434	Aptian-Albian	9.99	9.945	9.005	0.26	0.21	14.15	14.14	9.25	Pl. Chl	Temsamane
BMK-4	435848	3881340	Aptian-Albian	9.988	9.98	9.012	0.16	0.21	14.19	14.16	9.246	Pl. Chl	Temsamane
KH-1*	439246	3860751	Paleozoic	9.989	9.991	9.022	0.27	0.20	14.06	14.14	–	Pg. Chl. Hm	Kehbaba Kl.
KH-2M	439246	3860751	Berri.-Barrem.	9.980	9.977	9.027	0.28	0.19	14.15	14.14	9.273	Cc. Chl	Kehbaba Kl.
KH-2T	439246	3860751	Paleozoic	9.968	9.970	–	0.27	0.24	14.16	14.17	9.266	Chl. Cld	Kehbaba Kl.
KH-2P	439246	3860751	Triassic	9.980	9.975	9.022	0.26	0.16	14.15	14.14	9.270	Chl	Kehbaba Kl.
KH-3*	439344	3860860	Paleozoic	9.993	9.989	9.016	0.24	0.18	14.13	14.13	9.269	Pg. Chl. Kln	Kehbaba Kl.
KH-4*	439442	3862878	Berri.-Barrem.	10.006	9.994	9.018	0.50	0.41	14.15	14.14	9.271	Cal. Pg. Chl	Temsamane
KH-5	441499	3864757	Berri.-Barrem.	9.996	9.996	–	0.56	0.49	14.14	14.13	–	Cal. Chl	Temsamane
KH-6	440701	3866779	Berri.-Barrem.	9.989	9.989	9.020	0.45	0.37	14.14	14.14	9.271	Cal. Chl	Temsamane
KH-9	440311	3868137	Berri.-Barrem.	10.003	10.008	9.020	0.28	0.21	14.12	14.14	9.273	Cal. Chl. Cld	Temsamane
KH-10	440328	3868041	Berri.-Barrem.	10.003	10.001	9.022	0.32	0.23	14.15	14.14	9.273	Cal. Chl. Cld	Temsamane
KH-13	440496	3867883	Aptian-Albian	9.996	9.993	–	0.39	0.36	14.14	14.13	–	Chl	Temsamane
KH-14	440391	3869974	Berri.-Barrem.	9.987	9.991	9.036	0.31	0.22	14.14	14.15	9.272	Cal. Chl. Cld	Temsamane
KH-15	452279	3874008	Aptian-Albian	9.986	9.986	9.037	0.29	0.23	14.16	14.15	9.272	Cal. Chl. Cld	Temsamane
KH-16*	446896	3876790	Berri.-Barrem.	9.979	9.977	9.033	0.27	0.28	–	–	9.272	Pg. Chl/Smc	Temsamane
KH-17*	446862	3877669	Berri.-Barrem.	9.977	9.984	9.025	0.28	0.20	14.13	14.14	–	Cal. Pg. Chl	Temsamane
KH-18*	446537	3878063	Berri.-Barrem.	9.986	9.989	9.038	0.25	0.19	–	–	9.273	Cal. Pg	Temsamane
KH-19*	445899	3878263	Berri.-Barrem.	9.979	9.977	9.030	0.26	0.19	–	–	9.273	Pg. Chl/Smc	Temsamane
KH-20	445411	3879054	Aptian-Albian	9.972	9.968	9.031	0.22	0.18	14.15	14.14	9.272	Cal. Chl	Temsamane
KH-21*	444886	3879708	Aptian-Albian	9.980	9.984	9.020	0.25	0.19	–	–	9.272	Pg. Chl/Smc	Temsamane
KH-22*	443967	3881313	Berri.-Barrem.	9.980	9.975	9.026	0.33	0.23	–	–	9.270	Pg. Chl/Smc	Temsamane
KH-23	443340	3881965	Berri.-Barrem.	9.970	9.967	9.050	0.22	0.14	14.16	14.18	9.272	Cal. Pg. Chl. Cld	Temsamane
AMR1	435228	3863081	Berri.-Barrem.	–	10.029	9.018	0.21	0.32	14.18	14.14	9.270	Cal. Chl. Ab	Ait Amrâne Kl.
KHB	439246	3860751	Paleozoic	9.996	9.99	–	0.32	0.26	–	–	–	Chl	Kehbaba Kl.
TSM-0	439321	3854362	Paleozoic	9.969	9.965	9.001	0.19	0.19	–	–	–	Pg. Chl. Kln	Kehbaba Kl.

Mineral abbreviations according to Kretz (1983). Chl/Smc = Chlorite/Smectite mixed layers; Ill/Smc = Illite/Smectite mixed layers.
The high- and low-grade boundaries of the anchizone in the "CIS" scale are 0.25 and 0.42 Δ° 2Θ (Kisch et al., 2004).
*Samples where the illite crystallinity was measured on peak at 5 Å. On the rest of the samples the illite crystallinity was measured on the peak at 10 Å.
Berri.-Barrem. = Berriasian–Barremian.

Upper Miocene volcanic rocks crop out along the northern coast in the high-K calc-alkaline volcanoes of the Ras Tarf and Tres Forcas capes (Duggen et al., 2004, 2005). Messinian to Pliocene alkaline volcanic rocks related to the Gourougou stratovolcano crop out in the eastern part of the study area and in the sedimentary basins (Azdimousa et al., 2006; Duggen et al., 2004, 2005).

From north to south, the Temsamane fold-and-thrust stack consists of narrow anastomosing ductile shear zones thrusting over a lowermost unit deformed essentially by asymmetric south-vergent folds (Fig. 5). In the cross-sections, the shear zones have a hinterland-dipping duplex geometry with a roof shear zone at the base of the uppermost Ras

Afraou unit, dipping 15° NNW (Fig. 5). The lower imbricate shear zones dip 30–40° NNW (Fig. 5) and separate several tectonic units, from north to south, namely the Taliouine, Ijer–Jbel Mhajar, and Imzirene units (Figs. 4 and 5).

4.1. Upper units: Ras Afraou and Taliouine units

The upper units Ras Afraou and Taliouine units have been grouped by Azdimousa et al. (2007) into the Upper Temsamane unit, but in this work we will separate them due to the roof character of the Ras

Table 2
UTM coordinates of the samples studied by microbeam and for $^{40}Ar/^{39}Ar$ determinations.

| Sample	UTM (huse)	X	Y	Rock	Age of formation	Tectonic unit
NE-3	30 N	434665	3877451	Cld-schist	Berriasian–Barremian	Imzirene Unit (Temsamane U.)
NE-4	30 N	434665	3877451	Cld-schist	Berriasian–Barremian	Imzirene Unit (Temsamane U.)
K-3	30 N	456000	3893131	metabasite	Triassic–Jurassic	Taliouine Unit Temsamane U,)
TSM4	30 N	456000	3893131	metabasite	Triassic–Jurassic	Taliouine Unit Temsamane U,)
KH3	30 N	439344	3860860	phyllite	Paleozoic	Kehbaba Klippe
AMR-4	30 N	435228	3863081	metabasite	Triassic–Jurassic	Aït Amrane Klippe
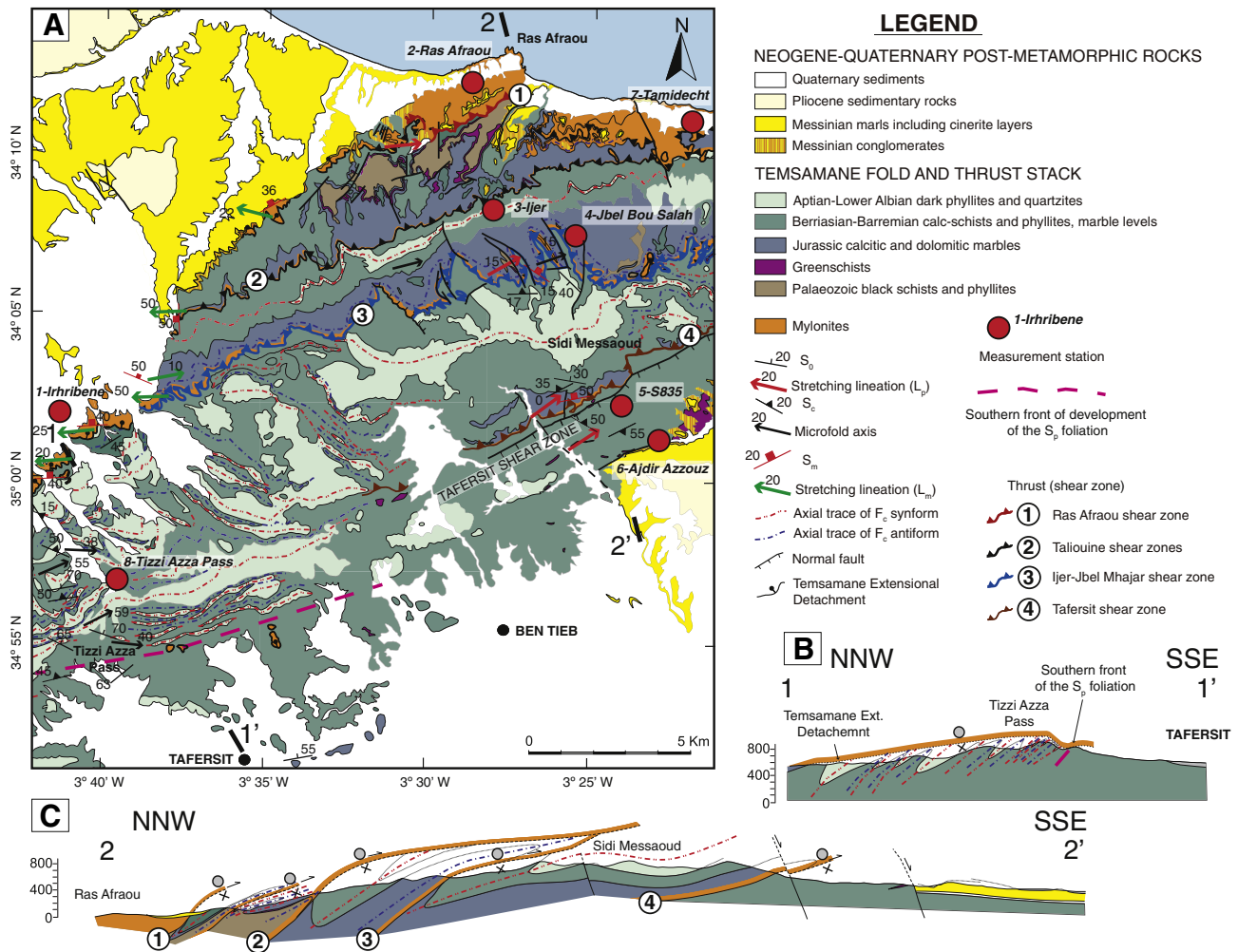
Fig. 5. Geological map and cross-sections of the northern sector of the central Temsamane fold-and-thrust stack. The structure includes the imbricated shear zones and part of the domain with south-vergent folds. See Fig. 4 for location. In the cross sections, the horizontal scale is the same than the vertical one.

Afraou unit and the fact that most of the published metamorphic and radiometric data are specifically located within this unit.

The uppermost Ras Afraou unit is characterized by a lithological sequence including Paleozoic rocks: black and gray fine-grained schists, phyllites, and quartzites, which are covered by Jurassic marbles. This tectonic unit includes chloritoid-bearing schists within the Paleozoic rock (Negro et al., 2007).

The internal structure of the Ras Afraou unit is composed by several asymmetric south-vergent folds with around one hundred meters of half-wavelengths and with the Jurassic marbles in the cores of the synclines in the Amjar area. These folds have hinges with ENE–WSW trends and axial surfaces dipping around 45° towards the NNW. The whole unit thrusts over the rest of the Temsamane units as the roof thrust.

The most visible fabric in this unit is a planar–linear fabric with a mylonitic foliation S_p and a stretching lineation L_p (Figs. 6 and 7A, B, C). The S_p mylonitic foliation in the Paleozoic metapelites is a schistosity defined by muscovite, paragonite, chlorite and chloritoid. Within the Jurassic marbles is a schistosity defined by muscovite, paragonite, and chlorite in M-domains alternating with calcite rich domains. In those marbles and in the Paleozoic schists, there are preserved microlithons where S_p deforms an older and crenulated foliation marked by decussate white micas. In most cases, the S_p foliation has a phyllonitic character and obliterates the old cleavage. Minor ductile shear zones deform the main foliation and produce ductile S-C and S-C′ structures. The main schistosity S_p is also deformed by a S_c discrete to zonal crenulation cleavage (Fig. 6).

The internal structure of the Taliouine unit is formed by the entire Temsamane metamorphic sequence, including Paleozoic to Lower Cretaceous rocks (Fig. 3). Its internal structure consists of two nappe sheets; the northern one includes a south-vergent syncline and an anticline, while the large-scale structure of the southern nappe includes three south-vergent F_c folds. The lowermost fold is an isoclinal anticline with a sheared reverse limb. The axial surfaces of the larger F_c folds have clear NW–SE strikes and NE dips, while the hinges have NW–SE trends (Fig. 7D and E). The F_c folds in these units have reverse limbs around 1 km long and develop an axial plane foliation (S_c, Azdimousa et al., 2007), while deforms the older S_p/L_p planar–linear fabric.

The main S_p foliation in the schists is similar to the previously described in the Ras Afraou unit, while in the metabasites under Green Schist facies of the Taliouine unit is defined by amphibole + epidote + albite + quartz + chlorite + biotite. There are also small C and C′ surfaces defined by chlorite + biotite cutting the S_p foliation (Sample TSM4, Fig. 6, Table 3) (see Azdimousa et al., 2007, for a photography and an outcrop interpretation near Imchiouene).

In the reverse limbs of the large inclined asymmetric F_c anticlines of the Taliouine unit and at the base of the Ras Afraou unit, the planar linear fabric is strongly penetrative and defines narrow shear zones cutting the axial surfaces of the F_c folds developed in their footwalls, which have a steeper dip (Fig. 5), we will describe them with most detail in the next subsection.

Fig. 7 represents the stereographic projections of the orientation of the main discussed structures: S_0 (Fig. 7A), S_p foliation (Fig. 7B) and L_p
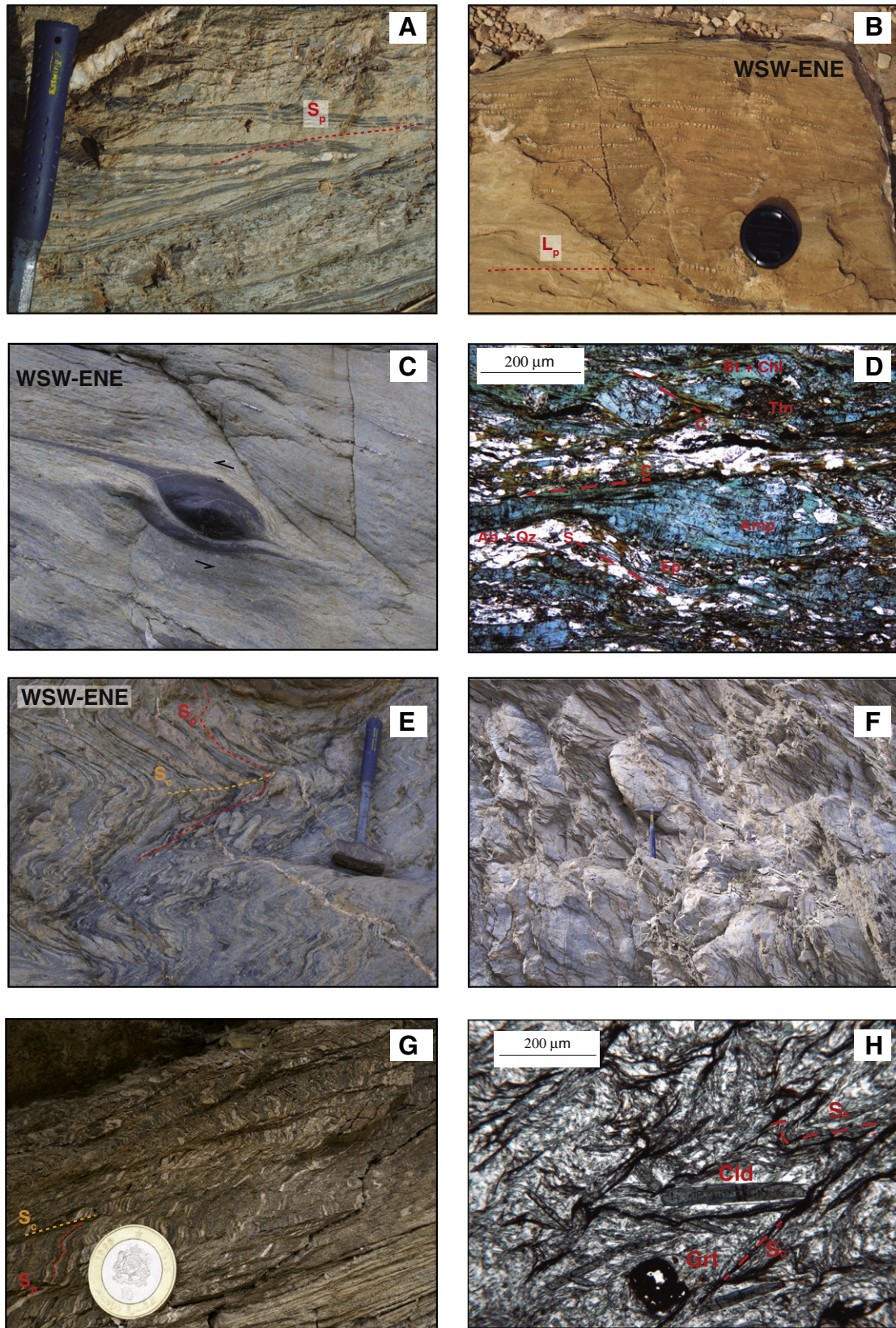
Fig. 6. Photographs illustrate the ductile meso and micro structures developed in the Temsamane fold-and-thrust stack. A) View of a minor F_p fold in the Aptian-Early Albian phyllites. B) View of the stretching lineation in the Jurassic marbles covering the Paleozoic rocks of the Khebaba klippe near Telat Atlef. C) Deformed black quartz nodule within the Berriasian–Barremian phyllites of the Imzirene unit. D) Thin-section of the TSM4 metabasite: Ab + Qz = albite + quartz , Amp = amphibole, Bt + Chl = biotite + chlorite, Ep = epidote, Ttn = Titanite, (see Fig. 4 for location, Table 2 for coordinates, Table 3 for composition). Abbreviations for minerals names after Whitney and Evans (2010). E) Type III interference pattern of Ramsay (1967) between the F_p and F_c folds in the Aptian–Early Albian dark phyllites. F) View of sheath folds developed in mylonites in Berriasian–Barremian whitish phyllites in the shear zone below the Temsamane detachment. G) View of the S_c crenulation cleavage in the Berriasian–Barremian phyllites of the Imzirene unit. H) Thin-section of the Berriasian–Barremian NE-4 Cld-bearing schists: Cld = chloritoid, Grt = pseudomorph after garnet (see Fig. 4 for location, Table 2 for coordinates, Table 4 for composition).
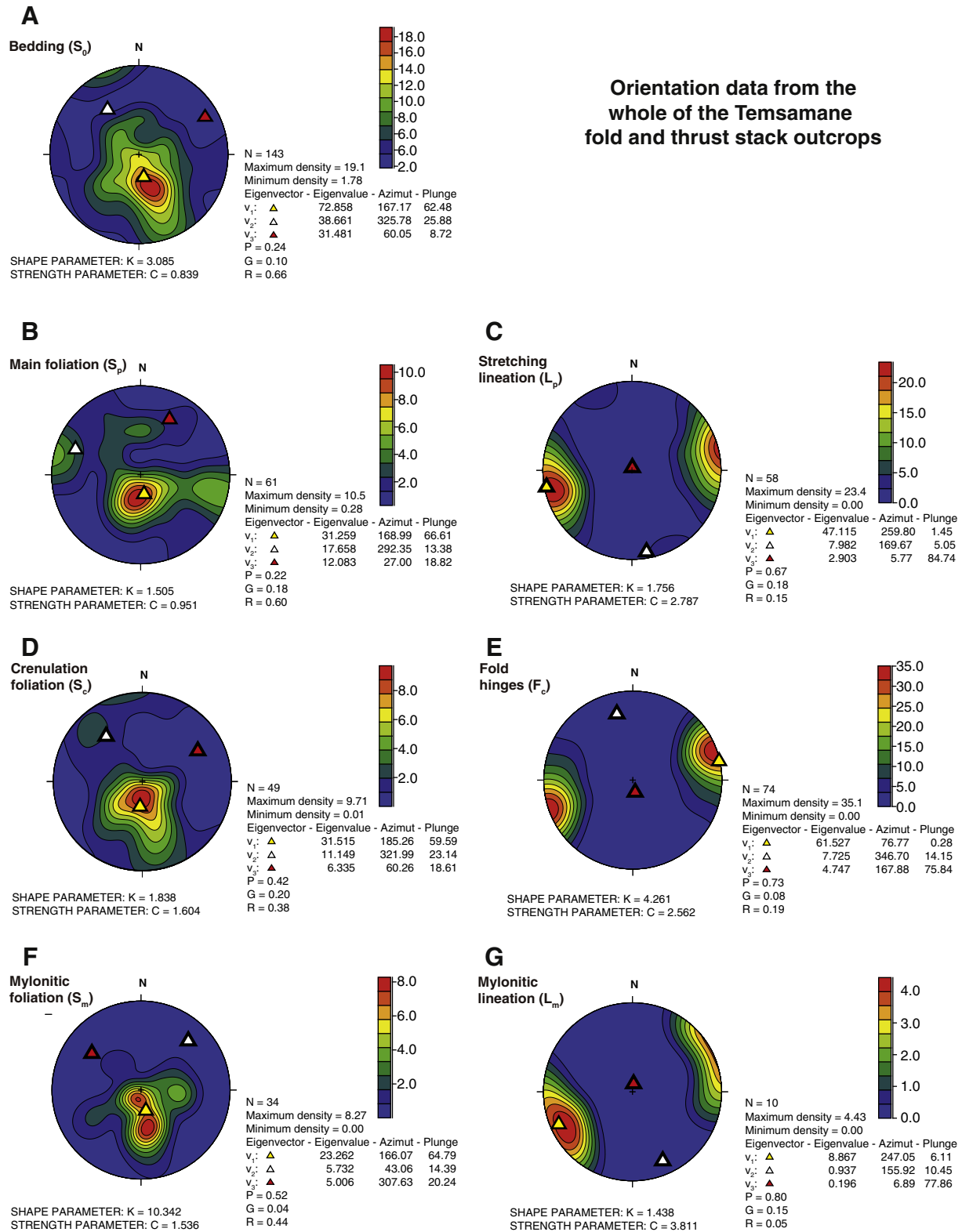
Fig. 7. Diagrams representing the orientation of the main ductile mesostructures in the metasediments of the study area: A) the bedding (S_0), B) main foliation (S_p), C) the associated stretching lineation (L_p), D) crenulation foliation (S_c) and E) the associated microfold hinges (F_c), and also F and G) the planar–linear fabric S_m/L_m cutting the reverse limbs of the fold-nappes. See text for the discussion about eigenvectors, eigenvalues and P, G, R, and C indexes. Wulff steronet, lower hemisphere.

stretching lineation (Fig. 7C), S_c (Fig. 7D) and F_c microfold hinges (Fig. 7E); while Fig. 8 presents the orientation data from different measurement stations. Eigenvectors (v_1, v_2, v_3) for every set of orientation data are marked (Fig. 7), as those eigenvector orientations derived

from orientation-tensor analysis of fabrics yields measures of the fabric shape (e.g., Woodcock, 1977). Furthermore, the P and G indices (point and girdle fabric indices respectively from Vollmer, 1990) are calculated. For each represented element of the fabric, the orientation tensor and its

Table 3

Representative analyses of minerals from sample TSM4. Minerals: Amp, amphibole (nomenclature after *Leake et al., 1997*); Ab, albite; Chl, chlorite; Bt, biotite.

Sample number	TSM4_C2_anf1	TSM4_C2_anf2	TSM4_C2_anf2	TSM4_C2_anf3	TSM4_C2_anf10	TSM4_C2_pl6	TSM4_C2_pist2	TSM4_C2_anf7	TSM4_C2_chlv2	TSM4_C2_chlm7	TSM4_C2_anf11	TSM4_C3_anf1pre	TSM4_C2_chlm3
Mineral	Amp	Amp	Amp	Amp	Amp	Ab	Ab	Ab	Chl	Chl	Chl	Chl	Bt
Analysis	265	266	269	270	291	280	281	282	276	290	295	297	284
SiO_2	54.51	53.63	54.56	55.18	53.99	66.84	66.17	67.06	27.03	27.14	28.32	27.51	40.43
TiO_2	0.05	0.03	0.02	0.02	0.05				0.03	0.03	0.09	0.02	0.76
Al_2O_3	2.77	3.22	3.16	2.31	2.67	19.25	18.93	18.85	20.03	19.57	19.41	19.77	12.57
FeO	11.01	12.48	11.38	11.00	12.37	0.14	0.36	0.12	17.41	17.94	16.65	17.97	13.95
MnO	0.15	0.14	0.14	0.16	0.14				0.17	0.20	0.14	0.16	0.06
MgO	16.59	15.53	16.05	16.82	15.80				21.10	20.87	21.09	20.97	15.73
BaO						0.00	0.00	0.00					
CaO	11.25	10.36	10.74	11.00	10.35	0.11	0.45	0.25	0.02	0.03	0.06	0.04	2.42
Na_2O	1.00	1.48	1.33	1.03	1.49	11.93	11.38	11.77	0.07	0.03	0.11	0.03	0.20
K_2O	0.10	0.11	0.10	0.07	0.11	0.08	0.10	0.10	0.06	0.05	0.56	0.02	6.45
	97.44	96.99	97.47	97.59	96.97	98.37	97.42	98.16	85.93	85.86	86.43	86.50	92.56
Structural formulae													
Si	7.71	7.65	7.72	7.77	7.70	2.98	2.98	2.99	2.79	2.81	2.89	2.82	3.04
Al	0.46	0.54	0.53	0.38	0.45	1.01	1.01	0.99	2.43	2.39	2.34	2.39	1.11
Aliv									1.21	1.19	1.10	1.18	
Alvi									1.22	1.20	1.24	1.21	
Ti	0.01	0.00	0.00	0.00	0.01				0.00	0.00	0.01	0.00	0.04
Fe^{2+}	0.91	0.93	0.95	0.83	0.92				1.50	1.55	1.42	1.54	0.88
Fe^{3+}	0.40	0.56	0.40	0.47	0.56				0.00	0.00	0.00	0.00	
Mn	0.02	0.02	0.02	0.02	0.02				0.02	0.02	0.01	0.01	0.00
Mg	3.50	3.30	3.39	3.53	3.36				3.24	3.22	3.21	3.21	1.76
Ca	1.71	1.58	1.63	1.66	1.58	0.01	0.02	0.01	0.00	0.00	0.01	0.00	0.19
Ba													
Na	0.28	0.41	0.37	0.28	0.41	1.03	0.99	1.02	0.01	0.01	0.02	0.01	0.03
K	0.02	0.02	0.02	0.01	0.02	0.00	0.01	0.01	0.01	0.01	0.07	0.00	0.62
Amphibole names	actinolite	actinolite	actinolite	actinolite	actinolite								
XMg									0.68	0.67	0.69	0.67	0.67
XAn						0.01	0.02	0.01					
XAb						0.99	0.97	0.98					
XOr						0.00	0.01	0.01					

Measurement stations (see location in Fig. 5)
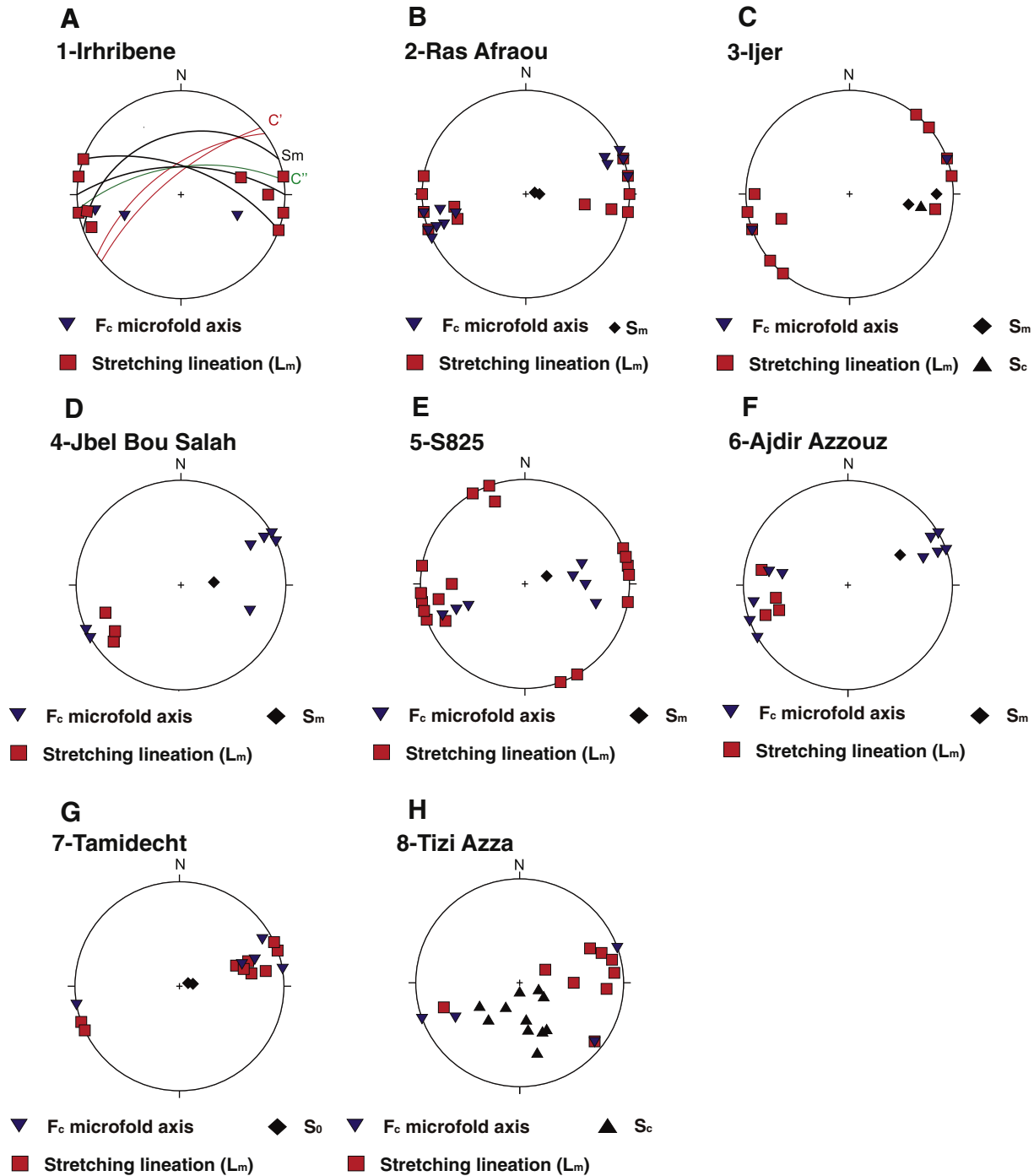
**Fig. 8.** Diagrams represent the stereographic projection of the orientation of the linear features in the measurement stations located in Fig. 5. Wulff steronet, lower hemisphere.

three eigenvalues E_1, E_2, E_3 are used to determine $P = (E_1 - E_2)/N$ and $G = 2(E_2 - E_3)/N$, where for a perfect point distribution the P and G values are 1.0 and 0 respectively, while for a perfect girdle distribution the P and G values are 1.0 and 0 respectively. Vollmer (1990) also defined an R index (random index: $R = 3E_3/N$) that measures how the data approach a perfect randomly distribution and

Fig. 9. Photographs of the ductile and brittle macro- and mesostructures developed in the Temsamane fold-and-thrust stack. A) View of the Jurassic marbles at the core of the major anticline at the base of the Ijer–Jbel Mhajar unit. See Fig. 5 for location at the measurement station 4–Jbel Bou Salah. B) Outcrop of the Imzirene shear zone where the Jurassic marbles thrust over the Berriasian–Barremian whitish phyllites. See Fig. 5 for location at the measurement station 5-S825. C) View of the S_m foliation in the Jurassic mylonitic marbles in the same outcrop. D) View of F_c folds in the normal limb of a major antiform in the Imzirene unit, near the locality of Ait Amrâne. E) Outcrop of the Aptian–Early Albian phyllites and quartzites near the Tizi Azza Pass. F) View of the S–C brittle–ductile structures deforming the Aptian–Albian phyllites and quartzites in the shear zone below the Temsamane detachment. G) Outcrop of the Temsamane detachment in the westernmost outcrops of the Temsamane fold-and-thrust stack (point 1 of cross-section1-1′ in Fig. 2). H) Photograph of one of a small extensional klippen of the Temsamane detachment north of the Ait Amrâne klippe. The Jurassic mylonitic marbles are over the whitish gauge derived from the Berriasian–Barremian phyllites.
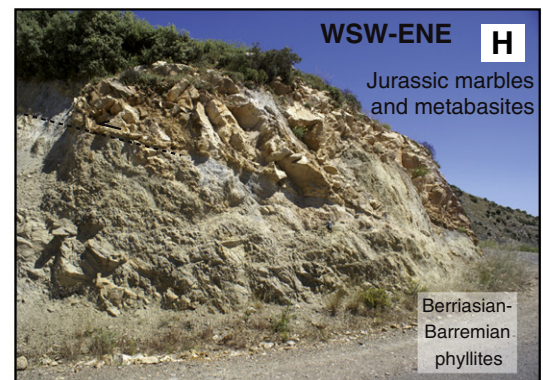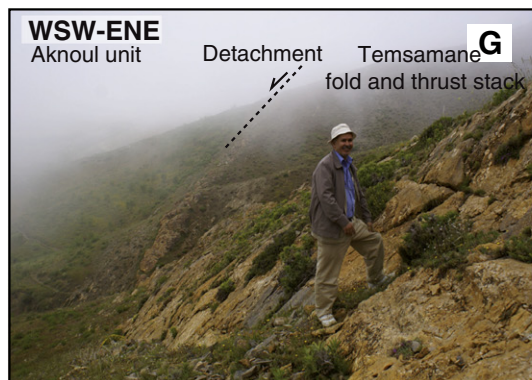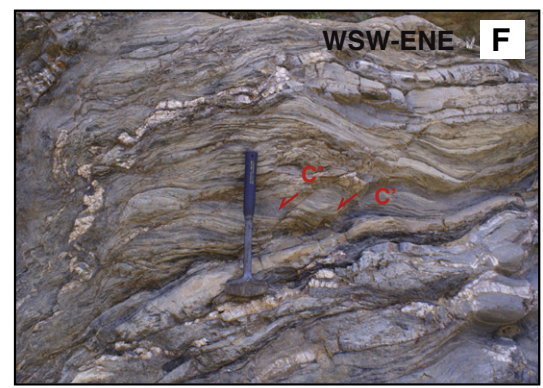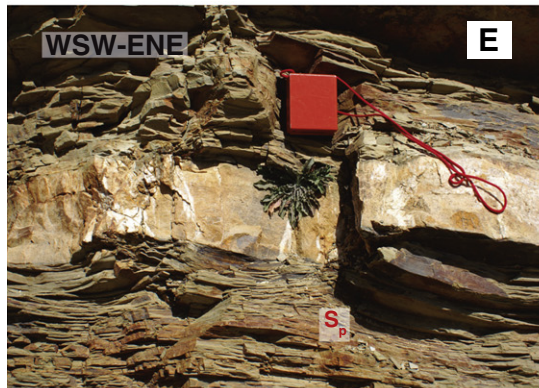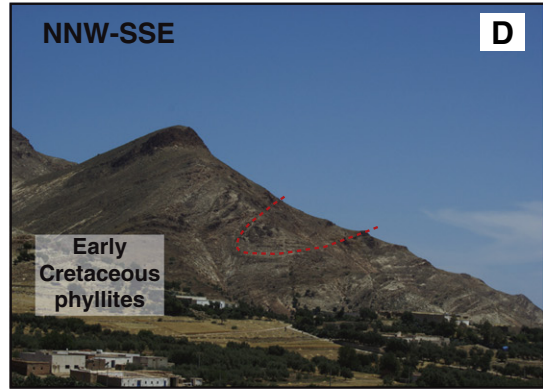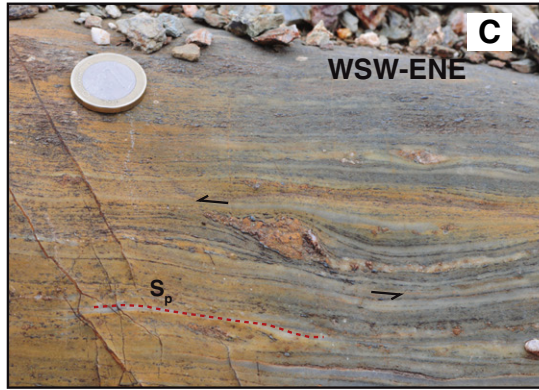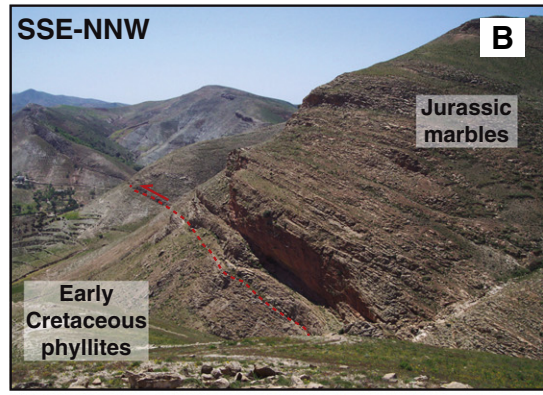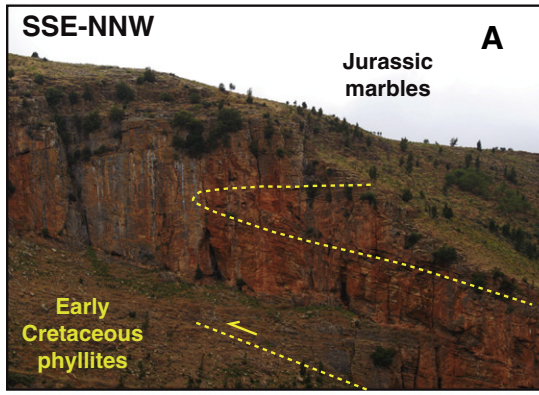
those three indices have the property that P + G + R = 1. Further-more, we include also the strength parameter C (C = ln (E$_1$/E$_3$)) proposed by Woodcock (1977), that ranges between 0 and infinity and that measures the fabric strength; i.e., higher values of C indicate strong preferred orientations.

The L$_p$ stretching lineation in the upper units has a fairly good point distribution with small dispersion (Fig. 7C). L$_p$ lineation has ENE–WSW trends with a mean orientation of 2° towards N80°E (Fig. 7C). The kine-matic indicators such as S-C, S-C′ structures, and σ and δ porphyroclasts indicate a top-to-the-WSW sense of shear (Fig. 6).

Most of the microfold hinges (75%) are sub-parallel to the L$_p$ stretching lineation although several measures (25%) are normal to L$_p$ or occur at angles between 20° and 50° from the lineation. This distribu-tion is not at random (R = 0.11) but follows a girdle on the S$_p$ surface (Fig. 7C). We also present the orientation data from different measure-ment stations in Fig. 8.

4.2. The intermediate unit: Ijer–Jbel Mhajar unit

The intermediate Ijer–Jbel Mhajar unit contains the whole Temsamane lithological sequence, ranging from Paleozoic to Early Cretaceous. The internal structure consists of two south-vergent F$_c$ folds: one large syncline with a core of Albian–Early Aptian quartzites and dark phyllites and one large inclined asymmetric anticline with a core of Paleozoic schists and Jurassic marbles (F$_c$ folds, Fig. 9). The ge-ometry and minor structures of these F$_c$ folds are similar to those of the Taliouine unit, but the folds are larger, with reverse limbs of more than 2 km long (Fig. 5). A 100 m-thick basal shear zone deforms and thins the reverse limb of the F$_c$ anticline and corresponds to the thrust over the lowermost Imzirene unit.

The succession of mesostructures is similar to that of the upper units: a S$_p$/L$_p$ planar linear fabric is the main fabric of the rocks and is deformed by the S$_c$ crenulation cleavage (Figs. 6 and 9). A younger S$_m$/L$_m$ mylonitic fabric develops within the basal shear zone of this unit. The S$_m$/L$_m$ planar–linear fabric developed in this shear zone is identical both in orientation and associated meso- and microstruc-tures from the S$_p$/L$_p$ fabric as indicated by the data of orientation from the S$_p$/L$_p$ fabric in the core of the major syncline (Ijer measure-ment station, Fig. 8), when compared with the data from S$_m$/L$_m$ pla-nar–linear fabric in the reverse limb of the Jbel Bou Salah anticline (Fig. 8). Combining the data of both stretching lineations, they follow a point distribution (P = 0.79) with a mean orientation of 6° of dip towards N247°E. However, the principle of cross-cutting relation-ships indicates that this shear zone was younger or coetaneous with the development of the F$_c$ folds as it deforms this reverse limb. Kinematic criteria as S-C structures also indicate a top-to-the-WSW shear regime.

Those younger shear zones define the basal thrusts of the Ras Afraou, Taliouine and Ijer–Jbel Mhajar units. The branch lines between the thrusts can be determined in the map (Fig. 4) and have approximately E–W trends. Those branch lines and the stretching lineation define an angle of around 20–30° opening west, indicating a strong left-lateral strike–slip component for those thrusts, which is also clearly indicated by the S-shape of the F$_c$ folds at the map scale.

4.3. Imzirene unit

The Imzirene unit is the southernmost and lowest unit of the Temsamane fold-and-thrust stack. It contains only Mesozoic rocks (Fig. 3) and extends southwards, including the outcrops of the so-called Tafersit and South Temsamane units defined by Frizon de Lamotte (1985, 1987) and Negro et al. (2007).

The lowermost shear zone (the Tafersit shear zone) crops out north-east of Ben Tieb, and is a 100-m-thick shear zone duplicating the Imzirene unit (Figs. 4 and 5). In the central part of the study area, the lowermost Tafersit shear zone cannot be recognized northwest of Ben

Tieb (Figs. 4 and 5). The large-scale structure consists of a train of 16 SE vergent F$_c$ folds (Fig. 5). Normal limbs are around 3 km long, and re-verse limbs have lengths varying from 1 to 2 km (Fig. 5). Minor folds with amplitudes of kilometers to hundreds of meters are common in both the limbs and hinges and, as the major F$_c$ folds, are tight to isoclinal angular folds with narrow hinge zones (Fig. 6).

There are two main structural domains in the unit: in the northern domain, the axial traces of the folds follow a sinusoidal pattern in the map between the Tafersit shear zone and the basal thrust of the Ijer–Jbel Mhajar unit defining mega S-C structures indicating a top-to-the-W sense of shearing with a left-lateral strike–slip component for those shear zones (Fig. 5). In the northern part of this domain, the axial sur-faces of the folds have E-W strikes, dips towards the north, and the basal thrust of the Ijer–Jbel Mhajar unit cut them at low angles. In the central part of the domain, the axial surfaces of the folds curve and have NW–SE strikes and dips towards the NE. In this central part, we can also observe opposite periclinal closures along the same axial surface producing flattened oval map patterns indicating NW–SE to WNW–ESE trends for the hinges of those folds. Furthermore, in the southern part, they curve again acquiring E-W strikes, dips towards the north and are cut by the Tafersit shear zone (Fig. 5). This central sector locates in the hinge of the youngest NE–SW very open vertical folds that we will dis-cuss in the next subsection.

In this northern domain, the S$_p$ foliation is a slaty cleavage defined by the orientation of white micas and chlorites. C and C′ surfaces are com-mon and cut the S$_p$ foliation indicating a top-to-the-W sense of shearing for the D$_p$ event. S$_c$ is zonal to discrete crenulation cleavage deforming the S$_p$ foliation.

The measured microfold data in this domain are consistent with a point distribution with a mean trend around N80°E, although N110 to N120°E trends are also measures, and no NW–SE can be observed in the area (Fig. 8).

The southern domain contains around 10 major F$_c$ folds with macro-scopic fold hinges with ENE–WSW orientation. The folds are open to tight, and the S$_c$ foliation is a slaty cleavage that is the only observable foliation in the rock. The S$_c$ foliation has an average orientation of ENE–WSW and dips around 30° towards the NNW. The L$_1$ intersection lineation between the bedding and the S$_c$ slaty cleavage has a mean 8/077 orientation (Figs. 5, 8, and 9). Minor fold hinges are sub-horizontal, trending ENE–WSW with a mean value of N80°E (Figs. 5, 8, and 9).

A transition zone between the two domains occurs in the southern slopes of the Tizi Azza Pass (south of parallel 34°55′N; Fig. 5). The front of the S$_p$ development has previously been interpreted as a thrust fault separating two different thrust sheets (Choubert et al., 1984). However, there are good outcrops along road P6201 from Tafersit to Boudinar, where the lithological sequence and the fold limbs are continuous and no fault rocks can be observed.

4.4. Later deformations

Locally, the south-vergent folds are deformed by open-to-tight F$_{c+1}$ folds with E–W trending hinges and sub-horizontal axial planes that produce meso- to macroscopic type III interference patterns (Ramsay, 1967) (Fig. 6). A S$_{c+1}$ zonal to discrete crenulation cleavage and a crenulation lineation with an E–W trend are associated with the folds.

The outcrops of the Temsamane fold-and-thrust stack are limited upwards by an uppermost ductile–brittle fault zone approximately 100 m thick: the Temsamane Extensional Detachment (Figs. 2 and 9) (Booth-Rea et al., 2012). These authors also describe the different out-crops of the detachment from east to west, including the westernmost outcrops where the fault surface dips 50° (see Fig. 9G). The detachment surface is deformed by NE–SW folds that we will describe latter in more detail, and in this work, we will focus on the outcrops of the central part of the Temsamane fold-and-thrust stack. In that area, the Temsamane

fold-and-thrust stack is cut by the detachment as a low-angle ductile shear zone approximately 100 m thick with a N45°E strike that dips 30–35°NW in the eastern border of the Boudinar basin (Figs. 4 and 5).

The detachment again crops out in the southwestern margin of the Boudinar basin as a ductile shear zone defined by mylonitic marbles separating the anchizonal Tanger–Ketama unit from the Imzirene unit (Fig. 9). The rocks have a strong planar–linear fabric that includes NE–SW trending stretching lineation with an associated top-to-the-SW movement (Booth-Rea et al., 2012) and sheath folds (Fig. 9). The Late Tortonian–Messinian sedimentary sequence of the Boudinar basin lays directly and unconformably over the mylonites.

The Ait Amrâne klippe has a lower sheet unit of mylonitic marbles and metabasites tectonically covered by diagenetic Cretaceous to Tertiary olistostromic sediments of the Aknoul units (Figs. 9 and 10). The whole sequence of sheet units is cut by E–W striking normal faults dipping south. The Telat Azlaf klippe has a similar sequence of tectonic units, whereas the Midar klippen are only composed of metamorphic rocks.

The Khebaba semi-klippe comprises of several layers of rocks beginning with chloritoid-bearing Paleozoic schists (Negro, 2005; Negro et al., 2007), metaconglomerates, and quartzites with bodies of metabasites overlain by red quartzites, conglomerates, and pelites attributed to the Triassic. Up section, there are mylonitic marbles attributed to the Jurassic that also include metabasite bodies. Diagenetic Cretaceous to Tertiary olistostromic sediments of the Aknoul units tectonically overlay the metamorphic sequence, except in the eastern and southeastern boundaries of the semiklippe, where recent transpressive structures have reversed this order (Fig. 10).

All these mylonitic rocks are limited downwards by brittle fault rocks: fault gauges and carbonated fault breccias. The striations measured in the fault zone at the base of the klippen have N80°E trends,

and cataclastic structures such as S-C structures and crushed clast trails indicate a WSW sense of movement of the hanging wall (Fig. 11).

The different orientations of the Temsamane extensional detachment indicates that this surface and all of these uppermost mylonitic rocks are folded by late folds. These late folds have NE–SW strikes and sub-vertical axial surfaces that are very open vertical folds with non-cylindrical geometries. The main mountain range is a NE–SW trending antiform with a slightly curved axial trace, its hinge zone locates within the northern domain of the Imzirene unit where the previously mega S-C structures develop. Considering one of that giant S-C structure as defined by two open folds, one anticline to the northwest and one syncline to the southeast, the younger anticlinal deforms the long limb rotating the F_c axial surfaces to NW–SE strikes and the hinges to NW–SE to WSW–ENE trends. Moreover, minor later folds produce Type III interference patterns (Ramsay, 1967) with hook-like cartographic patterns.

The late deformation recorded in the area are the NE–SW striking normal faults with dips towards the south in the border of the Kert basin (Azdimousa et al., 2007) that cut the folded detachment (cross sections in Figs. 5 and 10).

5. Metamorphism of the Temsamane fold-and-thrust stack

The metamorphism of the rocks from the Temsamane fold-and-thrust stack was studied in order to determine the mineral assemblages and the metamorphic conditions where the previously described deformations (see Section 4) took place.

We ran XRD analyses of 37 fine-grained metapelites from the study area: 29 from the Temsamane fold-and-thrust stack, 7 from the Khebaba klippen, and 1 from the Ait Amrâne klippe (Fig. 4, Table 1). The XRD data show that the principal phases in all samples are muscovite, chlorite, and quartz (Table 1), while calcite, plagioclase, paragonite,
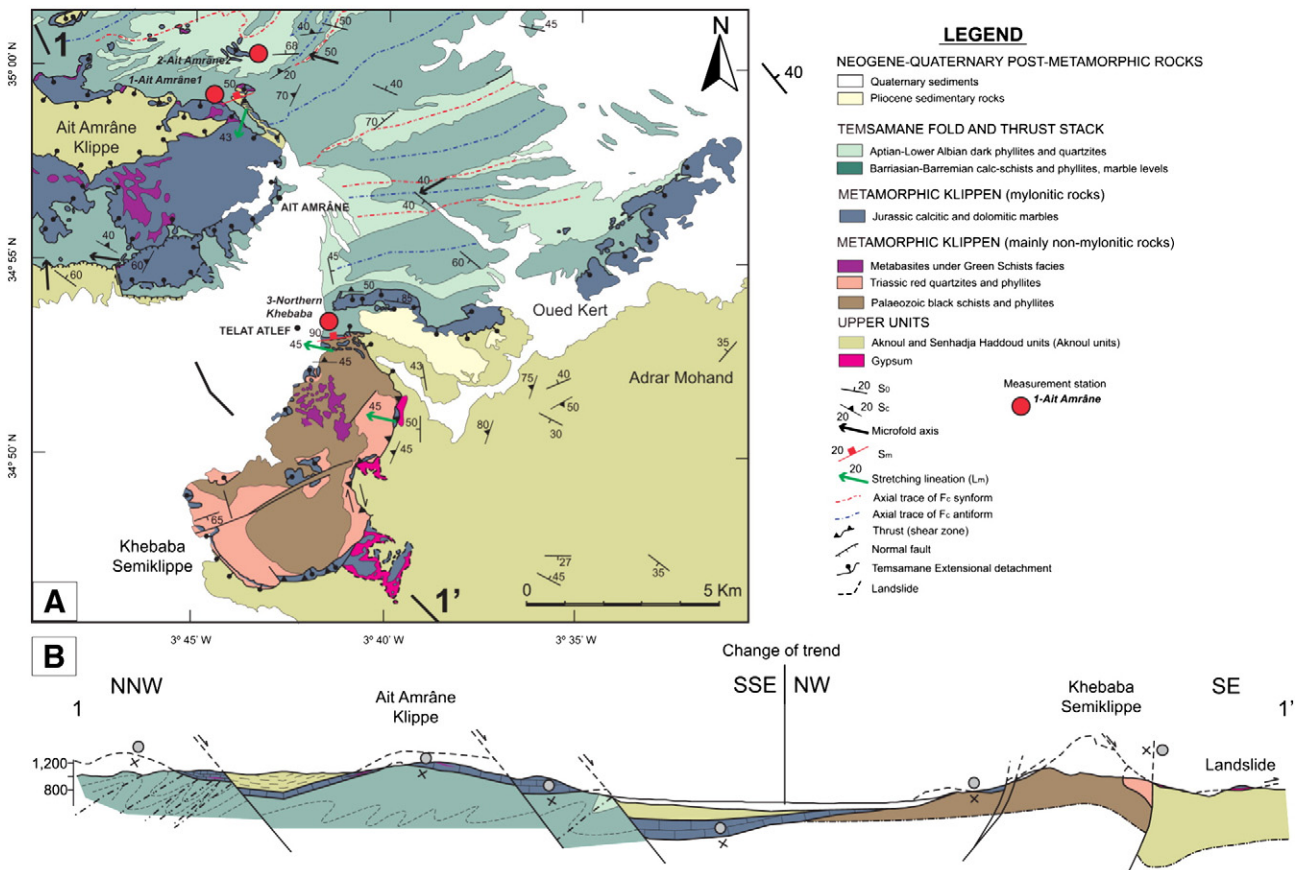

Fig. 10. Geological map and cross-section of the southern sector of the Temsamane fold-and-thrust stack including several of the large-scale extensional klippen (see Fig. 4 for location).

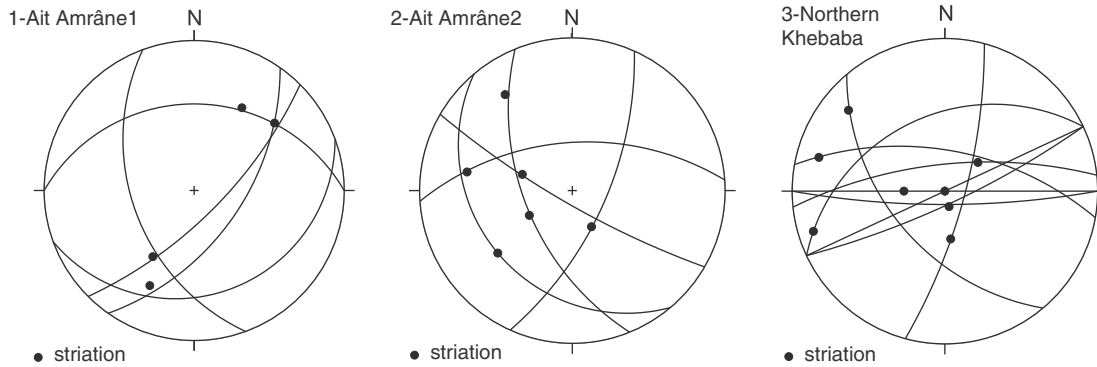**Measurement stations (see location in Fig. 10)**

Fig. 11. Diagrams representing the orientation of brittle mesostructures (striations and fault surfaces) in the fault gauges below the metamorphic klippen. See Fig. 10 for location of the measurement stations. Measurement station 2–Ait Amrâne corresponds to photograph 9H.

chloritoid, kaolinite, and hematite also form part of the mineral assemblages (Fig. 6, Table 1). Also smectite as part of chlorite-smectite mixed-layers (Chl/Smec) can be found in some samples.

5.1. Illite crystallinity

Illite crystallinity values are 0.56–0.16 Δ° 2 Θ, characteristic of late diagenesis to epizone conditions (according to Merriman and Peacor, 1999; see also Potel et al., 2006). Three samples from the Temsamane indicate high-diagenesis conditions (IC values >0.42 Δ° 2 Θ). They are located in the southern study areas, with the highest values in the Aptian–Lower Albian pelites at the core of southernmost F_c syncline of the Imzirene unit (Fig. 4). Fifteen samples from the Temsamane fold-and-thrust stack confirm anchizone metamorphic conditions (0.42–0.25 Δ° 2 Θ) essentially within the southern domain of the Imzirene unit (Fig. 4). Only two samples (KET-16 and KET-17*) are from the eastern outcrops of the Ras Afraou unit (Fig. 4). Eleven samples from the Temsamane fold-and-thrust stack indicate epizone conditions (0.25–0.16 Δ° 2 Θ), most from the northwestern extreme of the Temsamane outcrops. The seven samples from the Khebaba klippe and the sample from the Ait Amrâne klippe have IC values from epizone to high anchizone (0.33–0.20 Δ° 2 Θ) (Fig. 4, Table 1).

The illite crystallinity values determined both from the whole sample and the <2 μm fraction are very similar, with differences between IC <2 μm and IC whole lower than 0.10 (Table 1), indicating that there is little influence of detrital micas in the <2 μm fraction.

Mica basal spacing ranges from 8.997 to 9.038 Å (Table 1). An overall average of 9.02 Å (σ = 0.011) has been obtained for the b cell parameter. Samples from the Khebaba and Ait Amrâne klippen have b values of 9.001–9.027 Å, while the b values from the Temsamane fold-and-thrust stack are usually 8.997–9.038 Å. Most b values obtained (b > 9.02 Å) suggest a phengitic component of muscovite rather intermediate, which is characteristic of low heat flow in convergent settings (<25 °C/km; see Guidotti and Sassi, 1986; Stone and Merriman, 2004; Merriman, 2005). However, in some samples where the kaolinite has been identified, b values are low (8.997–9.007 Å, suggesting that they correspond to aluminous mica compositions as a consequence of the bulk-rock composition.

5.2. Chloritoid and paragonite

Chloritoid has been identified by XRD in eight samples, both in the Khebaba klippe and the Temsamane fold-and-thrust stack (Table 1). In other samples, it has been identified by optical microscopy and studied by microbeam analysis (sample NE-3; Fig. 6, Table 4). In the first samples, the mica basal spacing has not been measured due to the overlapping of the main peaks.

Paragonite has been detected in 16 samples both in the Khebaba klippe and the Temsamane fold-and-thrust stack (Table 1), indicating temperature conditions higher than 200 °C. In these Temsamane samples, the illite crystallinity was measured in the samples on the 5 Å muscovite peak.

Chloritoid and paragonite are distributed throughout the entire Temsamane fold-and-thrust stack outcrops, except for the southernmost outcrops of the Imzirene units with high diagenesis conditions (Table 1).

5.3. Kaolinite and smectite/chlorite mixed-layers

Kaolinite is present in five samples: the sample TEM-0 from the Khebaba klippe and samples KET-15, KET-16, KET-17*, and TEM-1* from the Ras Afraou unit (Table 1). Chlorite–smectite mixed-layers have also been determined in four samples, always coexisting with paragonite. In these cases, the chlorite has wide, poorly defined reflection peaks at 14 Å, reflecting low quantities and poor "crystallinity". Ethylene glycol solvatation of chlorite–smectite caused the appearance of 004 reflections at about 11.5 2θ and a broadening of the 003 and 004 reflections, and heating at 300 ° C caused a shift to 12 Å of the 14 Å reflection on the aggregates.

The co-existence of kaolinite with paragonite and/or chloritoid, which are thermodynamically incompatible phases, could be due to a retrograde-diagenetic origin for kaolinite and chlorite–smectite (Negro et al., 2007; Nieto et al., 2005), both in the Temsamane fold-and-thrust stack and in the Khebaba klippe.

6. ^{40}Ar/^{39}Ar results

^{40}Ar/^{39}Ar radiometric ages were determined in micas and amphiboles from rocks from the Temsamane fold-and-thrust stack and overlying units in order to constrain the ages of the deformational events and the associated metamorphic stages.

6.1. The Temsamane fold-and-thrust stack

Sample NE-4 is from a fine-grained chloritoid-bearing schist from the Imzirene unit with a Berriasian–Barremian depositional age. The sample NE-3 is located very close to the NE-4 sample and has a mineral assemblage: quartz + muscovite + paragonite + chlorite + chloritoid + rutile and round garnet pseudomorphs (Fig. 6). Muscovite + paragonite + chlorite + chloritoid define the main schistosity S_p, which is cut by the S_c discrete to zonal crenulation cleavage (Fig. 6). The chloritoid porphyroblasts have slight blue pleochroism and are Fe-rich (Fig. 6, Table 4), with X_{Fe} values of around 0.89–0.90 and X_{Mg} values of 0.06–0.07. Mn contents are high and the X_{Mn} is

Table 4

Representative analyses of minerals from sample NE-3 (Berriasian–Barremian whitish schists of the Imzirene unit). Minerals: Cld, chloritoid; Ms, muscovite; Pg, paragonite; Chl, chlorite.

Comment	N3_C1_ctd1	N3_C1_ctd4	N3_C1_ctd5	N3_C2_ctd1	N3_C2_ctd2	C3_chl19b	C5_mus5b	C5_mus7b	C6_mus3b	C1_mus5	C3_mus26b	C3_chl34b	C3_chl42b	C3_chl44b
Mineral	Cld	Cld	Cld	Cld	Cld	Ms	Ms	Ms	Ms	Pg	Pg	Chl	Chl	Chl
Analyses	106	117	118	125	126	117	240	244	256	114	135	152	169	171
SiO_2	23.96	24.07	23.83	23.75	23.89	47.83	46.34	46.52	46.08	45	44.78	23.14	23.28	23.23
TiO_2	0.01	0.01	0.07	0.38	0.01	0.11	0.1	0.1	0.13	0.75	0.07	0.03	0.06	0.04
Al_2O_3	38.00	38.34	38.07	38.62	38.60	32.93	32.69	32.37	32.18	34.19	34.75	21.28	21.31	21.36
FeO_t	27.41	27.50	27.95	26.79	27.01	3.43	4.05	4.11	3.73	2.39	5.9	33.8	33.33	33.71
MnO	1.28	1.32	1.41	1.51	1.21	0	0.01	0	0.01	0.02	0.09	0.54	0.75	0.57
MgO	1.01	1.09	1.03	1.05	1.07	0.68	0.9	1.02	0.79	0.46	1.13	8.47	8.37	8.38
CaO	0.01	0.01	0.00	0.01	0.00	0	0.05	0.01	0.02	0.03	0.04	0.01	0	0.01
Na_2O	0.05	0.01	0.01	0.01	0.01	1.99	0.76	0.83	1.58	3.43	5.29	0.01	0	0.01
K_2O	0.05	0.00	0.02	0.01	0.03	8.11	9.77	9.83	8.3	5.38	2.37	0.06	0.02	0.04
Cl	–	–	–	–	–	0	0.01	0	0	0.01	0.05	0.02	0.01	0.01
Total	91.80	92.37	92.42	92.13	91.86	95.07	94.69	94.79	92.82	91.65	94.47	87.35	87.13	87.36
Si	2.028	2.024	2.008	2.002	2.018	3.189	3.139	3.15	3.16	3.034	2.995	2.584	2.6	2.592
Ti	0.001	0.001	0.005	0.024	0.001	0.005	0.005	0.005	0.007	0.003	0.003	0.002	0.005	0.003
Al	3.792	3.801	3.781	3.839	3.842	2.587	2.61	2.583	2.601	2.925	2.739	2.801	2.805	2.808
Aliv	–	–	–	–	–	0.806	0.856	0.845	0.833	0.963	1.002	1.413	1.394	1.405
Alvi	–	–	–	–	–	1.781	1.754	1.738	1.768	1.962	1.737	1.388	1.411	1.404
Fe^{3+}	0.164	0.145	0.196	0.108	0.123	0.191	0.23	0.233	0.214	0.059	0.33	3.158	3.114	3.145
Fe^{2+}	1.776	1.789	1.773	1.781	1.785	–	–	–	–	–	–	–	–	–
Mn	0.092	0.094	0.101	0.108	0.086	0	0.001	0	0	0.002	0.005	0.051	0.071	0.054
Mg	0.128	0.137	0.130	0.132	0.136	0.067	0.091	0.103	0.081	0.027	0.112	1.41	1.394	1.394
Ca	0.001	0.001	0.000	0.001	0.000	0	0.004	0	0.001	0.006	0.003	0.001	0	0.001
Na	0.010	0.001	0.002	0.001	0.002	0.258	0.1	0.109	0.211	0.724	0.686	0.002	0	0.003
K	0.006	0.000	0.003	0.002	0.004	0.69	0.844	0.849	0.726	0.166	0.202	0.009	0.002	0.005
XMg	0.064	0.068	0.065	0.065	0.068	0.26	0.284	0.307	0.275	0.317	0.254	0.011	0.002	0.008
XFe	0.890	0.885	0.885	0.881	0.889	–	–	–	–	–	–	–	–	–
XMn	0.046	0.047	0.050	0.053	0.043	–	–	–	–	–	–	–	–	–

Table 5
$^{40}Ar/^{39}Ar$ analytical and age data on white mica crystals of sample NE-4 mu rr separated from one Cld-schist of the Imzirene unit (Fig. 4, Table 2).

Laser	Isotope ratios											
	NE-4 muscovite		(Sample/mineral)									
Power (%)	$^{40}Ar/^{39}Ar$	1σ	$^{37}Ar/^{39}Ar$	1σ	$^{36}Ar/^{39}Ar$	1σ	Ca/K	%^{40}Ar atm	f ^{39}Ar	$^{40}Ar*/^{39}ArK$	Age	2σ
2.20 W	9.45	0.10	0.05	0.06	0.030	0.002	0.09	94.77	0.15	0.494	5.36	±9.86
2.60 W	1.41	0.02	0.00	0.00	0.002	0.000	0.00	52.00	2.62	0.677	7.35	±0.94
3.20 W	1.11	0.01	0.00	0.00	0.000	0.000	0.01	13.13	20.49	0.963	10.44	±0.25
3.70 W	1.36	0.01	0.00	0.00	0.000	0.000	0.00	7.47	27.63	1.255	13.59	±0.19
4.20 W	1.41	0.01	0.00	0.00	0.000	0.000	0.01	7.77	15.03	1.301	14.09	±0.24
4.90 W	1.43	0.01	0.00	0.00	0.000	0.000	0.01	7.85	17.64	1.320	14.30	±0.19
5.70 W	1.47	0.01	0.00	0.00	0.000	0.000	0.01	8.26	10.77	1.349	14.61	±0.23
6.50 W	1.65	0.01	0.01	0.00	0.001	0.000	0.03	19.44	3.39	1.333	14.44	±0.47
7.50 W	1.96	0.02	0.03	0.01	0.002	0.000	0.06	34.85	1.67	1.276	13.82	±0.90
8.50 W	2.85	0.04	0.06	0.01	0.006	0.001	0.11	62.96	0.60	1.055	11.44	±3.28
Power (%)	$^{40}Ar/^{39}Ar$	1σ	$^{37}Ar/^{39}Ar$	1σ	$^{36}Ar/^{39}Ar$	1σ	Ca/K	%^{40}Ar atm	f ^{39}Ar	$^{40}Ar*/^{39}ArK$	1σ	
Total/Average	1.453	0.004	0.003	0.000	0.0003	0.0000			100.00	1.249	0.004	

J = 0.0060130 ± 0.0000301   Volume ^{39}ArK = 2.038   Integrated date = 13.54   ± 0.09   Ma
Plateau age = no plateau
Inverse isochron (correlation age) results. plateau steps: Model 1 Solution (±95%-conf.) on 8 points   Age = 14.14 ± 0.50 Ma
Initial $^{40}Ar/^{36}Ar$ = 286 ± 82   MSWD = 9.6   Probability = 0

0.04–0.05 (Table 4). The muscovites have Si^{4+} contents ranging between 3.09 and 3.20 a.p.f.u. with an average value of 3.15 a.p.f.u. (Table 4). Paragonites have Al^{3+} contents of 2.67 a.p.f.u., an average X$_{Mg}$ of 0.26, a mean Na value of 0.43 a.p.f.u. and a K of 0.42 a.p.f.u. Chlorite shows consistent compositions, with average X$_{Mg}$ values of 0.27 to 0.31 and Si contents in the range of 2.42–2.63 a.p.f.u.

Duplicate muscovite separates have been prepared from the NE-4 rock, and two analyses are reported: NE-4 mu (a) and NE-4 mu (b) (Tables 5 and 6). Neither analysis produced a clear plateau containing >50% of the ^{39}Ar (Fig. 12), one of the criteria for defining a plateau (McDougall and Harrison, 1999). However, age information can be gained from samples with complex geological histories by looking at chemical indicators in conjunction with the discordant age spectra (Negro et al., 2008).

Both analyses show a staircase age spectrum stepping up to around 15 Ma (Fig. 12). In NE-4 (a), 33.5% of the ^{39}Ar in four steps gives a weighted mean age of 14.41 ± 0.16 Ma (MSWD = 2.0), and the inverse isochron age is 14.14 ± 0.5 Ma (initial $^{40}Ar/^{36}Ar$ 286 ± 82, MSWD = 9.6). Comparison of the age spectrum with the Ca/K spectrum indicates that the three highest temperature steps have high Ca/K ratios (Figs. 12 and 13). This fact suggests a mica phase change or a different mica population

(Negro et al., 2008; Villa et al., 1997). The white micas in NE-3 have been identified as both phengites and paragonites, so we know that there is a mixed mica population in this rock. For the rest of the spectrum, the age changes with constant Ca/K, suggesting Ar loss from a homogeneous population (Negro et al., 2008). The second analysis NE-4 (b) has a similar age spectrum and analysis (Figs. 12 and 13). The high-temperature steps do not have high Ca/K ratios (Fig. 13), but the analysis may have been stopped before those temperatures were reached. The hottest six steps give a weighted mean age of 15.72 ± 0.28 Ma (35% of the ^{39}Ar, MSWD = 1.12), older than NE-4 (a) by 1 Ma, but neither is a precise age (Fig. 12). In both analyses (Tables 5 and 6), the staircase shape of the spectrum suggests a reheating event at around 6–8 Ma, while the 15–16 Ma age represents a minimum crystallization age. Moreover, micas in the NE-3 sample show Si content of about 3.15 (Table 4). These ages and the composition of the micas are in good agreement with the results from Negro et al. (2008) for the Ras Afraou unit.

Sample K3 is from an amphibolite from the Taliouine unit in the Imchiouene area, very near the location of TSM4. The rock is a very deformed sill-like body between the Paleozoic schists below and Jurassic marbles above. An amphibole separate from K3 has been prepared and produced a flat plateau age of 21.06 ± 0.46 Ma (Fig. 12, Table 7).

Table 6
$^{40}Ar/^{39}Ar$ analytical and age data on white mica crystals of sample NE-4 mu dup separated from one Cld-schist of the Imzirene unit (Fig. 4, Table 2).

Laser	Isotope ratios											
	NE-4 muscovite		(Sample/mineral)									
Power (%)	$^{40}Ar/^{39}Ar$	1σ	$^{37}Ar/^{39}Ar$	1σ	$^{36}Ar/^{39}Ar$	1σ	Ca/K	%^{40}Ar atm	f ^{39}Ar	$^{40}Ar*/^{39}ArK$	Age	2σ
2.20 W	4.94	0.06	0.08	0.04	0.013	0.002	−0.15	77.35	0.26	1.119	12.15	±11.56
2.60 W	1.19	0.01	0.00	0.00	0.002	0.000	0.01	40.52	3.67	0.705	7.66	±0.65
3.20 W	1.23	0.01	0.01	0.00	0.000	0.000	0.01	10.68	24.69	1.103	11.97	±0.17
3.80 W	1.42	0.01	0.00	0.00	0.000	0.000	0.01	6.97	33.97	1.323	14.35	±0.21
4.20 W	1.59	0.02	0.00	0.00	0.001	0.000	0.00	11.20	10.22	1.411	15.30	±0.50
4.90 W	1.61	0.01	0.00	0.00	0.000	0.000	0.00	9.55	7.15	1.457	15.80	±0.56
5.70 W	1.57	0.06	0.00	0.00	0.000	0.000	0.00	6.88	12.37	1.463	15.86	±1.19
6.50 W	1.57	0.01	0.00	0.00	0.000	0.000	0.00	6.57	5.22	1.468	15.91	±0.52
7.50 W	1.81	0.01	0.00	0.01	0.001	0.000	0.01	14.69	1.80	1.540	16.69	±1.21
8.50 W	2.03	0.02	0.01	0.04	0.002	0.001	0.02	24.50	0.65	1.536	16.65	±3.82
Power (%)	$^{40}Ar/^{39}Ar$	1σ	$^{37}Ar/^{39}Ar$	1σ	$^{36}Ar/^{39}Ar$	1σ	Ca/K	%^{40}Ar atm	f ^{39}Ar	$^{40}Ar*/^{39}ArK$	1σ	
Total/Average	1.462	0.004	0.004	0.000	0.0003	0.0000			100.00	1.219	0.005	

J = 0.0060220 ± 0.0000301   Volume ^{39}ArK = 1.345   Integrated Date = 13.23   ± 0.12   Ma
Plateau age = no plateau
Inverse isochron (correlation age) results. plateau steps: Model 1 Solution (±95%-conf.) on 6 points   Age = 15.67 ± 0.46 Ma
Initial $^{40}Ar/^{36}Ar$ = 301 ± 77   MSWD = 1.3   Probability = 0
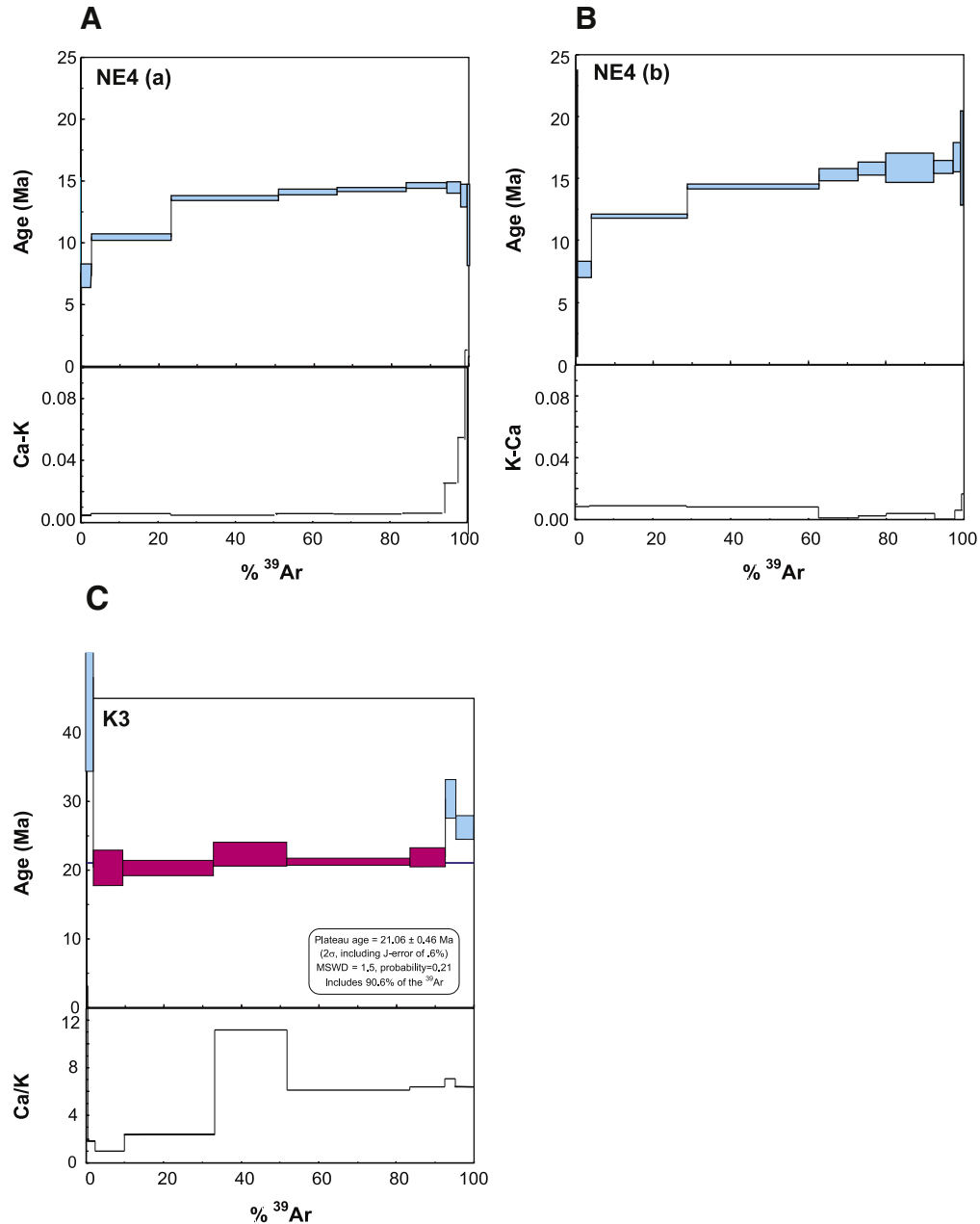
TEMSAMANE FOLD AND THRUST STACK

Fig. 12. Diagrams of cumulative ^{39}Ar Percent vs. Age (Ma) (upper part) and of ^{39}Ar Percent vs. Ca/K (lower part) of the samples from the Temsamane fold-and-thrust stack (see Fig. 4 for location, Table 2 for coordinates). In the upper part of every graphic, the plateau steps are magenta, the rejected steps are blue, and the box heights are 2σ.

A very old low-temperature step indicates the presence of excess ^{40}Ar that has been preferentially released at low temperature from non-retentive sites during deformation (McDougall and Harrison, 1999).

6.2. The Ait Amrâne and Khebaba klippes

Sample AMR-4 is from an amphibolite from the Ait Amrâne klippe and is a rock from a tabular body within the Jurassic marbles in the hanging wall of the klippe. An amphibole separate has been prepared from this rock and analyzed twice: AMR-4 amph (a) and the AMR-4 amph (b) (Tables 8 and 9). Both analyses produced age spectra with large errors in each step (Fig. 14). Both the low-temperature and highest-temperature steps are excessively old, the large errors in each step allow calculation of plateau ages for the two analyses that overlap

within the margin of error (Fig. 14); 76.1 ± 6.6 Ma and 82.4 ± 8.7 Ma, respectively (Tables 8 and 9). The average (78.3 ± 7 Ma) is a reasonable estimate of the age of the metamorphism of the rock.

Sample KH3 is from a Paleozoic phyllite from the hanging wall of the Khebaba klippe. Although white mica is the predominant mineral, the rock was too fine-grained for a good mineral separation. Instead, it was prepared as a whole rock, and the 0.25–0.175 mm fraction was analyzed twice: KH3 (a) and KH3 (b) (Tables 10 and 11).

Both analyses have staircase-shaped age spectra with no clear plateaus (Fig. 14), and unresolvable isochrons. Whole rocks contain a mixture of minerals and grain sizes that exhibit differing argon diffusion properties. They can be used for argon dating if the higher-temperature phases resolve to a plateau (McDougall and Harrison, 1999). Comparison of the age spectra with the Ca/K plots shows high Ca/K ratios at
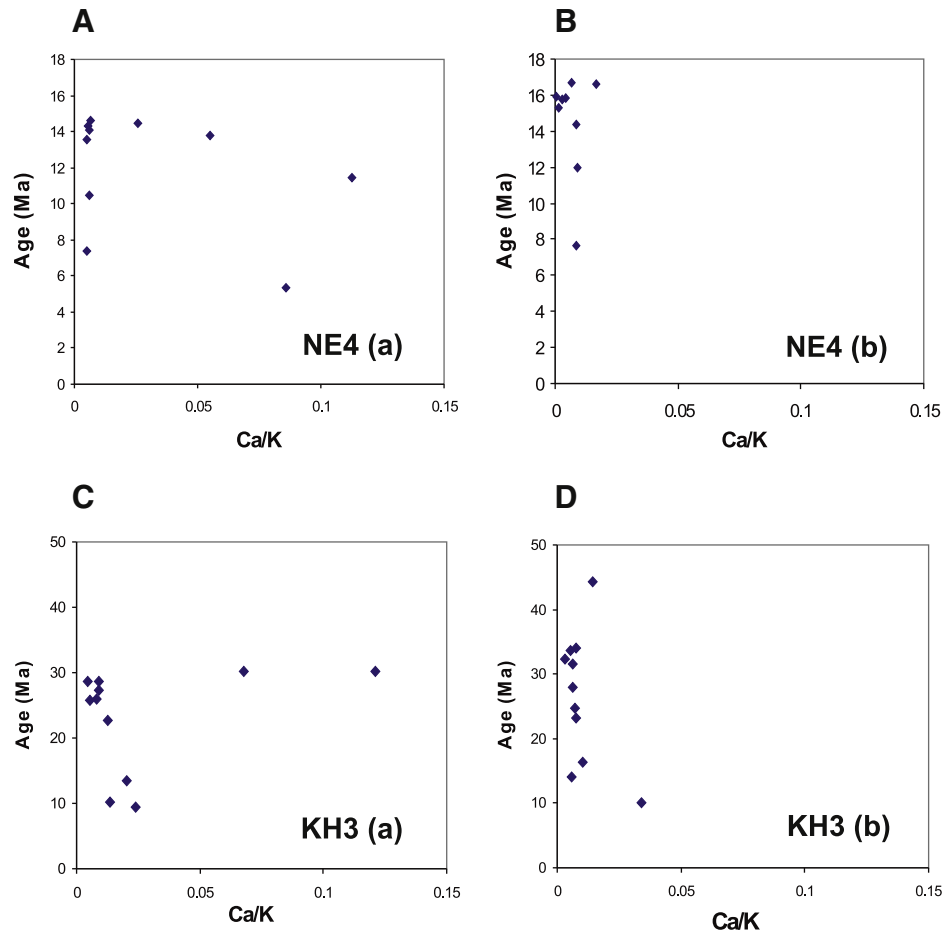
Fig. 13. Diagrams of cumulative ^{39}Ar Percent vs. Age (Ma) (upper part) and of ^{39}Ar Percent vs. Ca/K (lower part) of the samples from the metamorphic klippen (see Fig. 4 for location, Table 2 for coordinates). In the upper part of every graph, the plateau steps are magenta, the rejected steps are blue, and the box heights are 2σ.

the lowest and highest temperature steps, indicating a complex geological history (Fig. 13). The age vs. Ca/K plots (Fig. 13) suggest a combination of Ar loss from a homogeneous mica population (differing ages for the same Ca/K value) and co-existing diachronic or heterochemical mica populations (linear covariance) (Negro et al., 2008). It is difficult to assign a precise age to this rock; the hottest step is also the oldest

at 44.2 ± 7 Ma but only represents 1.72% of the released Ar (Table 11), which is very small. However, the ages of the highest-temperature steps may represent a minimum for the time at which the earliest micas formed during metamorphism. In KH3 (a), the oldest two steps are 30.1 ± 2 Ma; and in KH3 (b) the average of four steps is 33.3 ± 2 Ma (Tables 10 and 11), which suggests that the metamorphism

Table 7
^{40}Ar/^{39}Ar analytical and age data on amphibole crystals of sample KE3 separated from one metabasite under Green Schists facies of the Taliouine unit (Fig. 4, Table 2).

Laser	Isotope ratios											
	K3 amphibole				(Sample/mineral)							
Power (%)	^{40}Ar/^{39}Ar	1σ	^{37}Ar/^{39}Ar	1σ	^{36}Ar/^{39}Ar	1σ	Ca/K	%^{40}Ar atm	f ^{39}Ar	^{40}Ar*/^{39}ArK	Age	2σ
2.00 W	54.98	157.35	70.55	200.74	1.715	5.059	135.98	911.01	0.00	469.299	0.00	±17558
2.50 W	33.40	0.26	1.01	0.04	0.098	0.002	1.86	86.58	2.05	4.487	48.11	±13.73
3.00 W	4.45	0.05	0.54	0.02	0.009	0.000	0.99	58.00	7.53	1.871	20.22	±2.56
3.60 W	3.00	0.04	1.30	0.03	0.004	0.000	2.38	37.88	23.35	1.864	20.14	±1.13
4.10 W	3.00	0.02	6.09	0.10	0.005	0.000	11.20	31.66	18.91	2.058	22.22	±1.75
4.80 W	2.53	0.02	3.35	0.06	0.003	0.000	6.15	23.13	31.68	1.952	21.09	±0.55
5.60 W	2.84	0.02	3.49	0.08	0.004	0.000	6.40	29.26	9.11	2.017	21.78	±1.40
6.50 W	3.62	0.06	3.87	0.16	0.004	0.000	7.10	22.41	2.76	2.815	30.33	±2.81
8.00 W	2.94	0.04	3.49	0.10	0.003	0.000	6.41	17.72	4.60	2.423	26.13	±1.73

Power (%)	^{40}Ar/^{39}Ar	1σ	^{37}Ar/^{39}Ar	1σ	^{36}Ar/^{39}Ar	1σ	Ca/K	%^{40}Ar atm	f ^{39}Ar	^{40}Ar*/^{39}ArK	1σ
Total/Average	2.964	0.010	1.249	0.015	0.0036		0.0001		100.00	2.012	0.018

J = 0.0060090 ± 0.0000300   Volume ^{39}ArK = 0.428   Integrated Date = 21.61   ±0.43   Ma

Plateau age = 21.06 ± 0.46 Ma   (2 s. including J-error of .6%)   MSWD = 1.5. probability = 0.21   Includes 90.6% of the ^{39}Ar   steps 3 through 6

Inverse isochron (correlation age) results. plateau steps: Model 1 Solution (±95%-conf.) on 6 points   Age = 20.6 ± 1.5 Ma

Initial ^{40}Ar/^{36}Ar = 318 ± 35   MSWD = 3.4   Probability = 0.08

Table 8
^{40}Ar/^{39}Ar analytical and age data on amphibole crystals of sample AMR-4 amph separated from one metabasite under Green Schists facies of the Ait Amrâne klippe (Fig. 4, Table 2).

| Laser | Isotope ratios | | | | | | | | | | | |
| Power (%) | AMR-4 amphibole | | | (Sample/mineral) | | | | | | | | |
	^{40}Ar/^{39}Ar	1σ	^{37}Ar/^{39}Ar	1σ	^{36}Ar/^{39}Ar	1σ	Ca/K	%^{40}Ar atm	f ^{39}Ar	^{40}Ar*/^{39}ArK	Age	2σ
2.20 W	7921.97	2640.77	21.08	9.18	27.032	9.038	39.20	100.79	0.07	63.144	−862.42	±7478.63
2.60 W	2176.04	99.74	31.46	2.64	7.196	0.381	58.93	97.43	0.56	57.119	533.44	±930.16
3.10 W	485.40	16.41	25.42	1.42	1.463	0.065	47.40	88.16	2.20	58.545	544.93	±206.66
3.60 W	70.11	0.76	24.06	0.86	0.220	0.007	44.83	89.40	12.01	7.560	80.31	±44.00
4.10 W	44.01	0.39	30.95	0.63	0.132	0.004	57.96	82.22	32.19	7.998	84.86	±21.06
4.80 W	41.36	0.35	31.10	0.62	0.124	0.003	58.23	81.84	38.52	7.679	81.55	±17.77
5.50 W	19.56	0.14	34.45	0.79	0.051	0.002	64.68	61.40	8.50	7.739	82.17	±11.60
6.50 W	30.12	0.52	32.77	1.29	0.073	0.004	61.44	61.38	5.95	11.908	124.94	±25.24
Power (%)	^{40}Ar/^{39}Ar	1σ	^{37}Ar/^{39}Ar	1σ	^{36}Ar/^{39}Ar	1σ	Ca/K	%^{40}Ar atm	f ^{39}Ar	^{40}Ar*/^{39}ArK	1σ	
Total/Average	26.372	0.122	30.424	0.327	0.0856	0.0013			100.00	8.229	0.395	

J = 0.0060070 ± 0.0000300   Volume ^{39}ArK = 0.026   Integrated Date = 87.62 ± 8.17 Ma
Plateau age = 82.4 ± 8.7 Ma   (2 s. including J-error of .6%)   MSWD = 0.025. probability = 0.995   Includes 91.2% of the ^{39}Ar   steps 4 through 7
Inverse isochron (correlation age) results. plateau steps: Model 1 Solution (± 95%-conf.) on 8 points   Age = 79 ± 26 Ma
Initial ^{40}Ar/^{36}Ar = 305 ± 20   MSWD = 3.6   Probability = 0.001

may have at least this age. Here, the staircase shape of the spectra also suggests a reheating event at around 10–15 Ma, while the 30–33 Ma age represents a minimum crystallization age.

7. Discussion

7.1. Deformations in the Temsamane fold-and-thrust stack

The lithological sequences of the Temsamane fold-and-thrust stack include a Paleozoic basement and a Jurassic to Early Cretaceous metasedimentary cover. Similarities with the lithological sequences of the Eastern Moroccan Meseta, which outcrops in the eastern end of the Middle Atlas in the Oujda mountains and plain (especially the lack of sedimentary rocks of Triassic ages), suggest that they once formed part of the North African paleomargin (Chalouan et al., 2008). According to Frizon de Lamotte (1985), Negro (2005) and Negro et al. (2007), the regional structure corresponds to seven stacked thrust sheets having sequences with normal polarity. However, the new structural data indicate that the Temsamane rocks are structured into four major tectonic units (Fig. 4), each one consisting of a trend of F_c folds cut by shear zones.

The Temsamane fold-and-thrust stack recorded at least two major penetrative deformations: (1) the D_p deformation event producing the S_p/L_p planar–linear fabric, and (2) the D_c deformation event producing the S_c crenulation cleavage, the F_c folds and the imbricated shear zones with its associated S_m/L_m fabric.

The D_p structures developed only in the central and northern parts of the Temsamane fold-and-thrust stack, specifically in the northern imbricate units and in the northern domain of the Imzirene unit. The S_p/L_p planar–linear fabric was generated in a non-coaxial regime with a top-to-the-WSW sense of shear as indicated by the different types of S-C structures and σ and δ porphyroclasts.

As described in the upper units, when we analyze data from one measurement station the L_p stretching lineation has a point distribution with small dispersion (Fig. 8) and a mean ENE–WSW trend. However, when considering the whole of the L_p measurements, most of the measurement grouped around a mean N80°E trend with a P = 0.66, and several of the data occur at high angles of this mean L_p orientation (Fig. 7C). This strong dispersion on the trend and dips of the L_p stretching lineation through the whole of the structure cannot be explained by the latter D_c folding, as most of the F_c hinges are parallel to the mean L_p trend (Fig. 7E), suggesting that this dispersion within the

Table 9
^{40}Ar/^{39}Ar analytical and age data on amphibole crystals of sample AMR-4 amph r separated from one metabasite under Green Schist facies of the Ait Amrâne klippe (Fig. 4, Table 2).

| Laser | Isotope ratios | | | | | | | | | | | |
| Power (%) | AMR-4 amphibole | | | (Sample/mineral) | | | | | | | | |
	^{40}Ar/^{39}Ar	1σ	^{37}Ar/^{39}Ar	1σ	^{36}Ar/^{39}Ar	1σ	Ca/K	%^{40}Ar atm	f ^{39}Ar	^{40}Ar*/^{39}ArK	Age	2σ
2.00 W	137.19	229.70	7.98	26.49	0.446	1.037	14.69	95.35	0.01	6.415	68.38	±4508.79
2.50 W	2522.29	83.24	20.12	1.76	8.296	0.336	37.39	97.01	0.32	76.553	684.15	±869.30
3.00 W	502.78	16.79	17.85	1.03	1.414	0.056	33.11	82.32	1.94	90.015	781.64	±139.59
3.50 W	203.86	8.27	14.27	0.64	0.632	0.029	26.41	90.45	4.15	19.662	201.88	±82.46
4.10 W	40.28	0.42	21.76	0.57	0.118	0.004	40.48	81.78	22.77	7.452	79.19	±21.55
4.80 W	40.94	0.52	26.14	0.59	0.122	0.003	48.78	81.82	28.46	7.581	80.53	±17.06
5.60 W	18.08	0.25	26.73	0.54	0.048	0.001	49.90	65.51	27.31	6.357	67.77	±9.29
6.00 W	21.28	0.39	29.48	0.74	0.053	0.002	55.15	61.70	5.39	8.324	88.24	±14.26
7.50 W	24.74	0.33	29.64	1.33	0.065	0.005	55.45	66.54	1.99	8.454	89.58	±29.13
9.00 W	31.37	0.23	36.17	0.72	0.074	0.002	67.98	58.63	7.67	13.317	139.17	±10.76
Power (%)	^{40}Ar/^{39}Ar	1σ	^{37}Ar/^{39}Ar	1σ	^{36}Ar/^{39}Ar	1σ	Ca/K	%^{40}Ar atm	f ^{39}Ar	^{40}Ar*/^{39}ArK	1σ	
Total/Average	27.133	0.129	24.862	0.239	0.0679	0.0009			100.00	8.846	0.271	

J = 0.0060070 ± 0.0000300   Volume ^{39}ArK = 0.045   Integrated Date = 94.84 ± 5.58 Ma
Plateau age = 76.1 ± 6.6 Ma   (2 s. including J-error of .6%)   MSWD = 1.8. probability = 0.12   Includes 85.9% of the ^{39}Ar   steps 5 through 9
Inverse isochron (correlation age) results. plateau steps: Model 1 Solution (± 95%-conf.) on 10 points   Age = 72 ± 37 Ma
Initial ^{40}Ar/^{36}Ar = 329 ± 37   MSWD = 14   Probability = 0
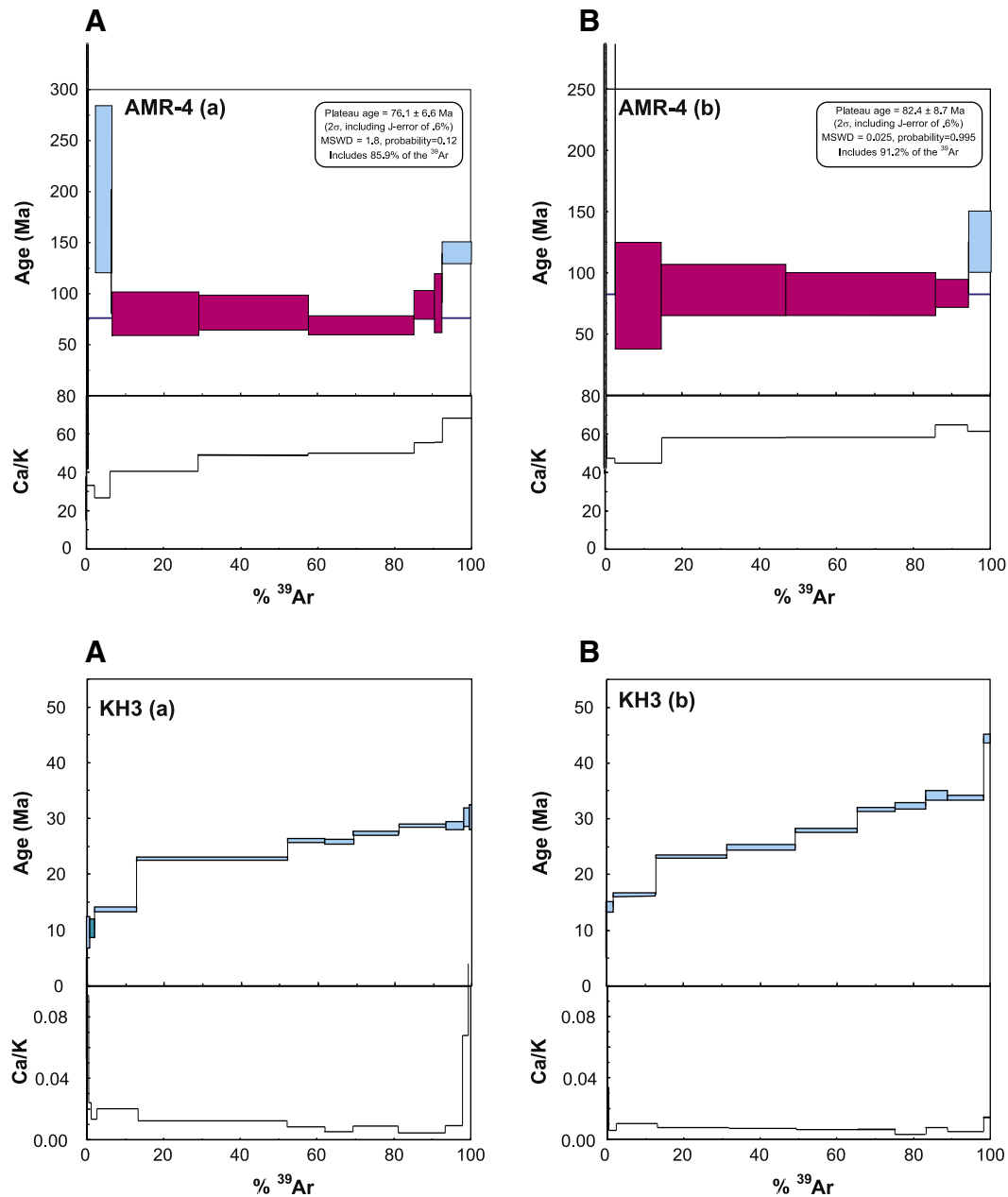
METAMORPHIC KLIPPEN

Fig. 14. Diagrams of Age (Ma) vs. Ca/K values from white micas in samples NE-4 and KH3. See text for discussion.

S_p foliation surface was an original characteristic of the S_p/L_p fabric. Similar fabrics containing a wide range of lineation orientations within the foliation plane, including lineations with opposite plunge senses, have been observed from several shear zones (Czeck and Hudleston, 2003; Díaz Azpiroz and Fernández, 2005; Sarkarinejad and Azizi, 2008). Furthermore, several models from transpressional shear zones can yield satisfactory explanations for some natural examples (see Fernández and Díaz-Azpiroz, 2009; Jiang, 2007). In summary, we propose that the S_p/L_p fabric was generated within a left-handed transpressional regime with a top-to-the-WSW sense of movement.

The D_p deformational event was followed by the D_c event, which generated the major structures of the Temsamane fold-and-thrust stack. Towards the north, there is a strong localization of non-coaxial ductile strain producing narrow ductile shear zones associated to the reverse limbs of recumbent fold-nappes that acted as thrust structures (Fig. 5). Towards the south, the Imzirene unit is composed essentially of sixteen asymmetric F_c folds, with only a minor shear zone (the Tafersit shear zone).

The geometry of the imbricate shear zones corresponds to a hinterland dipping duplex. The stretching lineation (L_m) within the shear zones has an average N80°E trend and an associated top-to-the-WSW sense of shear (Figs. 6 and 7) as indicated by the micro-, meso- and macro-structures as the mega S-C structures cutting the F_c folds developed in the northern domain of the Imzirene unit (Fig. 5). The angles between the shear zone branch lines and the stretching lineation are around 20° opening towards the west, indicating also a strong left-lateral strike–slip component of motion for the whole thrust stack, which is also indicated by the S-shape of the Fc folds at the map scale.

Table 10
^{40}Ar/^{39}Ar analytical and age data on white mica crystals of sample KH-3 mu separated from one phyllite of the Khebaba semiklippe (Fig. 4, Table 2).

| Laser | Isotope ratios | | | | | | | | | | | |
| | KH3 muscovite | | | (Sample/mineral) | | | | | | | | |
Power (%)	^{40}Ar/^{39}Ar	1σ	^{37}Ar/^{39}Ar	1σ	^{36}Ar/^{39}Ar	1σ	Ca/K	%^{40}Ar atm	f ^{39}Ar	^{40}Ar*/^{39}ArK	Age	2σ
2.00 W	130.81	81.55	1.11	7.82	1.242	1.040	−2.02	−280.42	0.00	497.219	2503.36	±2019.67
2.40 W	5.58	0.10	0.05	0.04	0.025	0.004	0.09	132.74	0.09	1.826	−19.99	±25.07
2.80 W	2.77	0.02	0.01	0.01	0.006	0.000	0.02	68.49	0.73	0.874	9.49	±2.75
3.20 W	1.53	0.01	0.01	0.00	0.002	0.000	0.01	38.64	1.41	0.942	10.22	±1.66
4.00 W	1.76	0.01	0.01	0.00	0.002	0.000	0.02	28.94	10.77	1.249	13.55	±0.44
3.60 W	2.25	0.02	0.01	0.00	0.000	0.000	0.01	6.95	39.09	2.098	22.68	±0.37
3.70 W	2.59	0.01	0.00	0.00	0.001	0.000	0.01	7.36	9.71	2.398	25.91	±0.35
4.00 W	2.57	0.01	0.00	0.00	0.001	0.000	0.01	7.16	7.41	2.384	25.76	±0.42
4.50 W	2.70	0.01	0.00	0.00	0.001	0.000	0.01	6.57	11.78	2.523	27.26	±0.37
5.20 W	2.81	0.01	0.00	0.00	0.000	0.000	0.00	5.73	12.26	2.651	28.62	±0.33
6.00 W	2.86	0.01	0.00	0.00	0.001	0.000	0.01	7.58	4.53	2.647	28.58	±0.70
7.00 W	3.20	0.02	0.04	0.00	0.001	0.000	0.07	12.60	1.55	2.795	30.16	±1.62
8.00 W	4.22	0.04	0.07	0.01	0.005	0.000	0.12	33.88	0.69	2.793	30.15	±2.30
Power (%)	^{40}Ar/^{39}Ar	1σ	^{37}Ar/^{39}Ar	1σ	^{36}Ar/^{39}Ar	1σ	Ca/K	%^{40}Ar atm	f ^{39}Ar	^{40}Ar*/^{39}ArK	1σ	
Total/Average	2.354	0.004	0.007	0.000	0.0005	0.0000			100.00	2.288	0.007	

J = 0.0060180 ± 0.0000301   Volume ^{39}ArK = 1.365   Integrated Date = 24.753 ± 0.15 Ma
Plateau age = no plateau
Inverse isochron (correlation age) results. plateau steps: Model 1 Solution (±95%-conf.) on 8 points   Age = 26.0 ± 4.2 Ma
Initial ^{40}Ar/^{36}Ar = 390 ± 210   MSWD = 25   Probability = 0

Similarities in the orientations, and shear regimes between D_p and D_c deformational events strongly suggest that they are the result of a unique deformational regime, where D_c was the evolution in time from D_p event. Concretely, the imbricated shear zones may account for localization of the shear strain into narrow bands cutting the lithological sequence, while the folds accommodated a sub-vertical shortening.

The major F_c folds have axial surfaces with low dips, fold hinges with ENE–WSW trends (Figs. 5, 6 and 7), and are SSE vergent. The large-scale anticlines at the base of these units are recumbent fold-nappes cut by shear zones with a stretching lineation sub-parallel to the anticline hinges. Ramsay et al. (1983) proposed that large-scale recumbent folds in the Helvetic nappes could be generated by the simple shearing of competent layers in the hanging wall of large thrusts. This model requires staircase geometry of the thrusts with ramps cutting across the competent layers where folds will nucleate. The geometry of the Temsamane thrusts cutting across the whole lithological sequence from the Paleozoic schists to the Aptian–Lower Albian quartzites accounts for the nucleation and development of the large-scale folds, but indicates that both the large scale folds and thrust shear zones most probably are related.

Recumbent folds with a stretching lineation parallel to the fold hinges are very common in orogens worldwide (see Bastida et al., 2014, and references therein). Bastida et al. (2014) review and discus the folding for recumbent folds and they proposed a mechanism for the formation of large-scale recumbent folds with a stretching lineation parallel to the fold hinge in areas with low metamorphism. This mechanism combines a deformation in a regime of simple shear, and a superposed coaxial strain with sub-vertical maximum shortening (Bastida et al., 2014), and as these authors propose, the development of the stretching lineation parallel to the fold axis is probably associated with the homogeneous strain superposed on the folds and not with the previous history of buckling. This mechanism can account for the left-handed transpressive deformational regime for the whole Temsamane fold-and-thrust stack. In fact, the presence of one superposed coaxial

Table 11
^{40}Ar/^{39}Ar analytical and age data on white mica crystals of sample KH-3 mu rr separated from one phyllite of the Khebaba semiklippe (Fig. 4, Table 2).

| Laser | Isotope ratios | | | | | | | | | | | |
| | KH3 mucovite | | | (Sample/mineral) | | | | | | | | |
Power (%)	^{40}Ar/^{39}Ar	1σ	^{37}Ar/^{39}Ar	1σ	^{36}Ar/^{39}Ar	1σ	Ca/K	%^{40}Ar atm	f ^{39}Ar	^{40}Ar*/^{39}ArK	Age	2σ
2.20 W	4.21	0.04	0.02	0.03	0.011	0.001	0.03	77.85	0.19	0.933	10.13	±4.98
2.60 W	2.56	0.02	0.00	0.00	0.004	0.000	0.01	49.10	1.76	1.303	14.12	±0.95
3.00 W	1.85	0.01	0.01	0.00	0.001	0.000	0.01	18.21	10.87	1.509	16.35	±0.31
3.50 W	2.38	0.02	0.00	0.00	0.001	0.000	0.01	9.86	18.59	2.144	23.18	±0.32
4.00 W	2.49	0.02	0.00	0.00	0.001	0.000	0.01	7.73	17.78	2.295	24.80	±0.47
4.50 W	2.75	0.02	0.00	0.00	0.000	0.000	0.01	6.15	16.07	2.581	27.87	±0.39
5.00 W	3.11	0.02	0.00	0.00	0.001	0.000	0.01	5.83	9.81	2.931	31.62	±0.39
5.70 W	3.19	0.03	0.00	0.00	0.001	0.000	0.00	6.42	8.05	2.988	32.23	±0.54
6.50 W	3.41	0.04	0.00	0.00	0.001	0.000	0.01	7.33	5.59	3.163	34.10	±0.85
7.50 W	3.32	0.02	0.00	0.00	0.001	0.000	0.01	5.92	9.57	3.119	33.63	±0.45
8.50 W	4.85	0.03	0.01	0.01	0.002	0.000	0.01	15.13	1.72	4.115	44.24	±0.74
Power (%)	^{40}Ar/^{39}Ar	1σ	^{37}Ar/^{39}Ar	1σ	^{36}Ar/^{39}Ar	1σ	Ca/K	%^{40}Ar atm	f ^{39}Ar	^{40}Ar*/^{39}ArK	1σ	
Total/Average	2.768	0.006	0.004	0.000	0.0006	0.0000			100.00	2.414	0.007	

J = 0.0060180 ± 0.0000301   Volume ^{39}ArK = 3.063   Integrated Date = 26.12 ± 0.14 Ma
Plateau age = No plateau
Inverse isochron (correlation age) results. plateau steps: Model 1 Solution (±95%-conf.) on 11 points   Age = not resolved

strain with sub-vertical maximum shortening was most likely responsible for the formation of the F_{c+1} folds and their associated sub-horizontal S_{c+1} crenulation cleavage. Such asymmetric small-scale folds with sub-horizontal axial surfaces and unrelated with the major folds are called Christmas-tree folds and are common in orogens that have experienced gravitational-experienced collapse (see Fossen, 2010).

The sub-vertical maximum shortening is also coherent with the movement of the Temsamane extensional detachment (Booth-Rea et al., 2012). In map view and in a cross-section parallel to the stretching lineation (Figs. 2, 4, and 5), the Temsamane extensional detachment has low-angle ramp geometry that cuts down into the fold-and-thrust stack, completely omitting the Ras Afraou, Taliouine, and Ijer–Jbel Mhajar units and partially omitting the Imzirene unit. These tectonic units are covered by tectonic klippen of metamorphic rocks (e.g., Ait Amrâne and Khebaba klippen). Among these klippen, the Khebaba unit also underwent IP-IT metamorphism (7–9 kbar and 380–430 °C, Negro et al., 2008), similar to the more internal Temsamane units, and may represent an extensional duplex detached from the Ras Afraou or a similar unit and transported to its present day location. The fact that the diagenetic shales of the Aknoul units tectonically overlie those metamorphic klippen indicates that low-angle normal faults stepped down into the detachment towards the south, omitting the intermediate anchizonal Tanger–Ketama unit.

The presence of the Temsamane detachment in the roof of the Temsamane fold-and-thrust stack can explain most of the thinning of the intermediate part of the orogenic wedge: Tanger–Ketama and Aknoul units (Booth-Rea et al., 2012), and also the unroofing and cooling of the Temsamane fold-and-thrust stack. Moreover, it could also explain the strong thinning of the continental crust of the eastern Rif belt, which can reach around 22 km in thickness, compared to about 42 km in the western Rif (Mancilla et al., 2012; Gil et al., 2014).

7.2. IC values from the Temsamane fold-and-thrust stack

In the southern Imzirene unit, IC values indicate late diagenetic conditions (0.56–0.45 °2Θ), whereas the central outcrops reach values corresponding to low- to high-anchizone conditions (0.45–0.28 °2Θ) (Fig. 4, Table 1). The IC values also increase towards the north in the Imzirene unit, from high anchizone to epizone conditions in the front of the S_p foliation to clear epizone values in its northern extreme (0.28–0.21 °2Θ). According to the estimations of Merriman and Frey (1999), the transition from late diagenesis to low anchizone occurs at ~200 °C and from high anchizone to epizone at ~300 °C in a normal gradient (25–30 °C/km). However, the comparison between the determined IC values and the estimated metamorphic conditions in regions that underwent HP-LT events followed by an increase of temperature during the decompression path as the Alpujárride Complex in the Betic Chain (Spain), Verrucano Group in the Apponienes (Italy), the Puncoviscana Fm from the Eastern Cordillera (Argentine), among others, produce several unresolved problems (e.g., Do Campo and Nieto, 2003, and references therein). However, those problems do not present in terrains that underwent HP–LT events followed by a decompressive path without increase of temperatures (Potel et al., 2006). These latter authors determined temperatures for rocks that underwent HP–LT metamorphism at 230 ± 10 °C for the late diagenesis to low anchizone transition, at 295 ± 10 °C for transition from high anchizone to epizone, and around 350 °C for IC values of 0.15 within the epizone conditions.

Negro et al. (2007) estimated geothermal gradients of 13–15 °C km^{-1} for the studied rocks, lower than the normal gradient and also clockwise P–T–t paths with nearly isothermal decompression after the peak pressures. The determined low gradients are also consistent with the b values in white micas obtained in this work (b > 9.02 Å) that, as previously described, are characteristic of low heat flow in convergent settings (<25 °C/km; see Guidotti and Sassi, 1986; Stone and

Merriman, 2004; Merriman, 2005). Moreover, the nearly isothermal decompression allow us to use the transition temperatures from Potel et al. (2006), and therefore, we can estimate that the Imzirene unit underwent peak temperatures around 230 ± 10 °C in its southern domain, between ~230 and ~295 °C in its central part, and higher than 295 ± 10 °C in its northern domain during the D_p event producing the recrystallization of the white micas.

The chlorite–smectite mixed-layers are stable through a range of temperatures between 150 and around 300 °C (Schiffman and Fridleifsson, 1991, and references therein). These mixed-layers minerals are only observed in the central part of the Imzirene unit also suggesting temperatures lower than 300 °C in this area. Furthermore, temperatures higher than 200 °C in the whole Temsamane fold-and-thrust stack and the Khebaba klippen are also indicated by the distribution of paragonite in the entire study area.

The northern units (Ras Afraou unit), the metamorphic klippen and the rocks of the Imzirene unit directly below the Beni-Malek ultramafics have IC values within the epizone conditions, which are also in accord with the estimated peak metamorphic conditions by Negro et al. (2007) with temperatures of 330–430 °C and 7–9 kbars in the Ras Afraou unit, the Tres Forcas Cape outcrops, and the Khebaba klippe.

As previously described in section 5.3, kaolinite coexists with thermodynamically incompatible phases as paragonite and/or chloritoid in the rocks with epizone conditions from the Ras Afraou unit and the Khebaba klippen, suggesting a latter retrograde event with diagenetic conditions superposed on the previous metamorphic event (Negro et al., 2007; Nieto et al., 2005).

7.3. Age determinations and implications for the evolution of the Eastern Rif

The estimated P–T conditions by Negro et al. (2007) range between temperatures of 330–380 °C and pressures of 7–8 kbars for the Ras Afraou rocks, suggesting that the temperatures of the northern Temsamane fold-and-thrust stack never surpassed 450 °C (tc closure temperature for the $^{40}Ar/^{39}Ar$ system in amphiboles, see Harrison, 1981) and therefore the 21.06 ± 0.46 Ma plateau age for the amphiboles of the K-3 rock can be interpreted as the growing age of these minerals and not a cooling age below 450 °C.

Monie et al. (1984) have analyzed by the $^{40}Ar/^{39}Ar$ method an amphibole separate from a sample of a metabasite under Green Schist facies from the same outcrop, near Taliouine. They have found an age spectrum with large error in every step and without a plateau. They interpret an age of around 28.2 ± 6 Ma for the low temperature steps as result of the metamorphic crystallization of the amphibole, and an age around 132.4 ± 13.3 Ma for the higher temperature steps, interpreted as the result of a heritage of the pre-metamorphic evolution of the rock. Azdimousa et al. (1998) have found two K/Ar ages on micas from the Tanger–Ketama Unit at 126.6 ± 2.1 to 131.9 ± 3.2 Ma respectively and they interpreted it as the age of the extensional metamorphism of the Tanger–Ketama rocks (see Vázquez et al., 2013, in press, and references therein). This Cretaceous extensional metamorphism has been discussed (see Michard et al., in press and Vázquez et al., in press, respectively a comment and reply on the work of Vázquez et al., 2013, in press). However, the finding of foliated metamorphic clasts of Middle–Upper Jurassic formations from the External Rif included within Berriasian–Barremian sedimentary breccias by Benzaggagh et al. (2013, their Fig. 7) and Benzaggagh (in press) clearly indicates the existence of this Cretaceous metamorphism and also the exhumation and erosion of the resultant ductile deformed metamorphic rocks during Early Cretaceous times.

The previous data suggest that the Temsamane lithological sequence may also underwent the same extensional metamorphic event during their paleomargin stage. However, in our data, the entire heritage has been erased and only the metamorphic plateau age rested indicating an Aquitanian age for the metamorphism associated to the D_p event.

Monie et al. (1984) determined one $^{40}Ar/^{39}Ar$ age in white micas of 27.8 ± 0. Ma, which is very close to the aforementioned age of 28.2 ± 6 Ma for the low temperature steps in amphiboles. Negro et al. (2008) also determined $^{40}Ar/^{39}Ar$ ages in white micas from the Ras Afraou unit and Tres Forcas Cape outcrop and found several ages between 23 and 33 Ma, which they interpret as the age of the IP–IT metamorphism. In summary, these ages strongly suggest that the D_p deformational event and the IP–IT metamorphic conditions took place essentially in the Aquitanian and it possibly begun in the Oligocene. Furthermore, the orogenic wedge of the north Maghrebian paleomargin in the eastern Rif was built essentially at that time (Fig. 15). The age of 21 Ma for the metamorphism in the orogenic wedge of the north Maghrebian paleomargin also correspond to a major thermal event which affected the Alpujárride–Sebtide in the Internal Zone of both the Rif and Betics (see Rossetti et al., 2010 for review).

The $^{40}Ar/^{39}Ar$ ages in white micas from NE-4 are around 15 Ma, which agrees with most of the $^{40}Ar/^{39}Ar$ ages in micas determined by Negro et al. (2008). Negro et al. (2008) interpret this age as the generation of the muscovite mica defining the main rock foliation. IC index values at the vicinity of NE-4 range between 0.16 and 0.26 Δ° 2θ, and as previously mentioned they correspond to temperatures between 295 and 350 °C according to Potel et al. (2006). These range of temperatures are just below the t_c for the $^{40}Ar/^{39}Ar$ system in

micas (up to 450 °C, see Harrison et al., 2009), and we interpret this age as representing the growth of the white micas in the Imzirene unit. The fact that the amphiboles crystallized at 21 Ma at 330–380 °C while the micas grew below 450 °C at ~15 Ma, indicates that during 6 Ma rocks the fold-and-thrust stack maintained at almost the same temperature suggesting that the orogenic wedge of the north Maghrebian paleomargin was stable during this period (Fig. 15). From Aquitanian to Langhian times, the Temsamane rocks remained in conditions of intermediate crust without significant vertical uplifting movements and cooling stages.

The Ait Amrâne klippe over the Temsamane fold-and-thrust stack is composed mainly of Jurassic marbles and metabasites under Green Schist facies that are covered by detached fragments of the Aknoul units. $^{40}Ar/^{39}Ar$ analysis of amphiboles from the metabasite indicates that the rocks cooled below 450 °C at 76.1 ± 6.6 Ma (Campanian times).

Vázquez et al. (2013, in press) present metamorphic data from the Tanger–Ketama unit that show that these rocks have undergone extensional metamorphism related with thinning of the continental crust that exhumed the Beni-Malek peridotites. The K/Ar radiometric ages in micas of the Tanger–Ketama unit range from 131.9 ± 3.2 Ma to 78.0 ± 1.2 Ma (Azdimousa et al., 1998, 2003), dating this extensional metamorphic event as Cretaceous (Leikine et al., 1991; Vázquez et al., 2013, in press). The old radiometric ages of the metamorphic rocks of
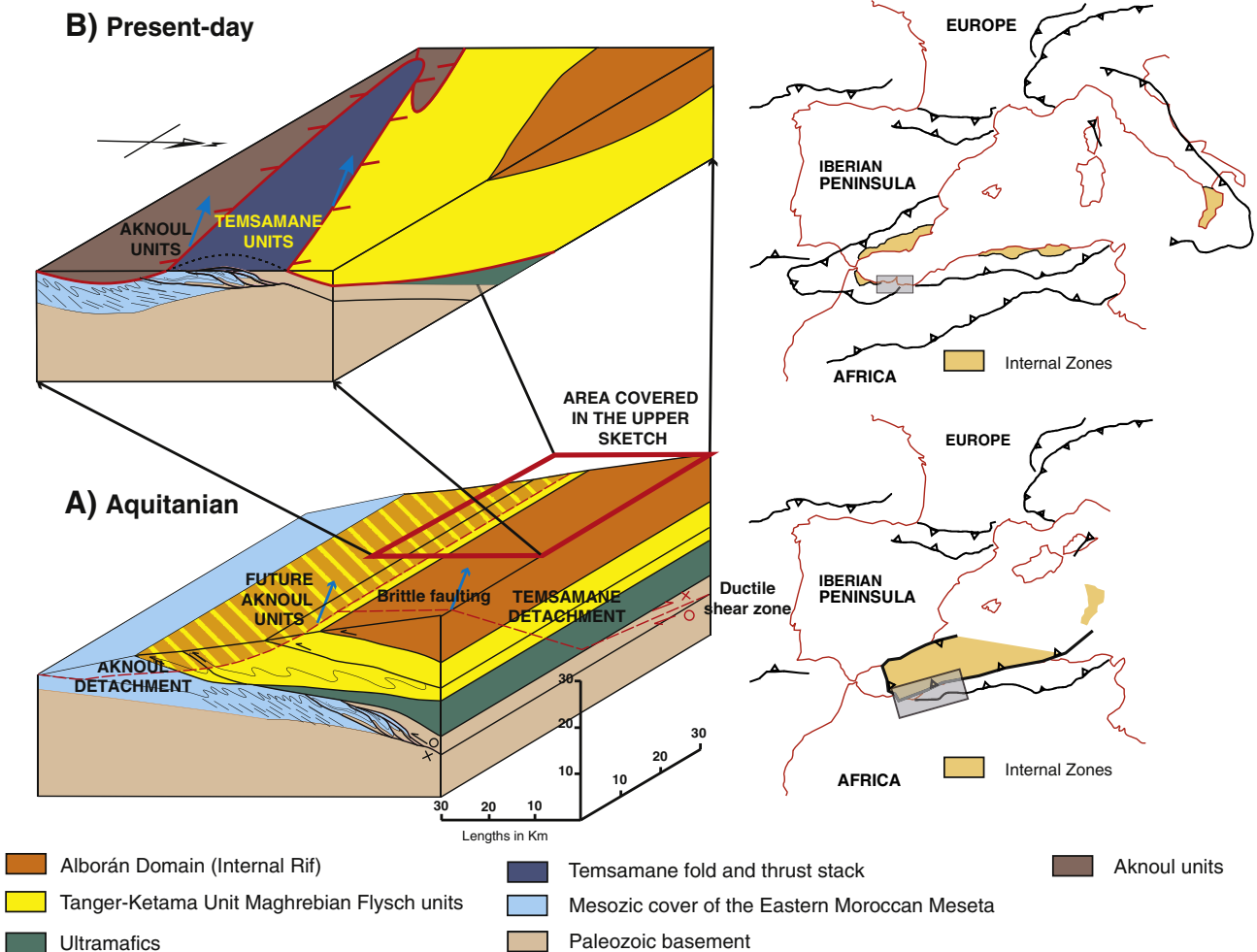

Fig. 15. Block diagrams illustrating the tectonic evolution of the studied area from Aquitanian times (A) to present-day (B). Both block diagrams show at their right side a tectonic sketch of the Western Mediterranean area. The tectonic sketch at Aquitanian times includes a reconstruction of the deformational front of the Alpine chains and the approximate location of the Internal zones of Rif, Betic, Kabilyas and Peloritan chains. A) Block diagram of the orogenic wedge of the Rif Chain formed at Aquitanian times (the gray rectangle in the Aquitanian tectonic sketch). Discontinuous red lines in the block diagram mark the location of the future Aknoul and Temsamane detachments, while the blue arrows mark the sense of movement of their hanging walls. B) Block diagram of the present-day structure of the eastern Rif, which corresponds to a part of the area represented in A (the gray rectangle in the corresponding present-day tectonic sketch).

the Ait Amrâne klippe determined in this work are explained if this klippe was a fragment of the Jurassic sequence of the Tanger–Ketama unit thinned by the action of the Temsamane detachment.

The Khebaba klippe includes several superposed tectonic units, below which are chloritoid-bearing Paleozoic rocks (Negro et al., 2007, 2008) whose KI values also indicate epizone metamorphic conditions. The ^{40}Ar-^{39}Ar age of micas from sample KH-3 indicates that the HP–LT metamorphic event was at least from an age between 30 and 33 Ma, which is similar to those ages obtained by Monié et al. (1984) and Negro et al. (2008) from the Ras Afraou unit and Tres Forcas Cape outcrop (between 23 and 33 Ma). As previously discussed, Negro et al. (2008) estimated IP–IT conditions at 7–9 kbar and 380–430 °C for the metamorphic conditions of those Paleozoic rocks, similar to the uppermost Temsamane units, and this klippen may represent an extensional duplex detached from the Ras Afraou or a similar upper Temsamane unit.

Sealing Upper Tortonian–Lower Messinian conglomerates and marls in the Boudinar Basin are 7.1–6 Ma in age (Azdimousa et al., 2006), helping to constrain the age of the exhumation and unroofing of the Temsamane fold-and-thrust stack. Negro et al. (2008) have also interpreted ^{39}Ar-^{40}Ar ages of 10–6 Ma as the age of clay minerals that developed during extension. These data suggest that the D_c deformational event took place during the Langhian–Early Tortonian, when the Temsamane fold-and-thrust stack underwent significant vertical uplifting (Fig. 15). One possible cause was that the Middle Atlas rocks were accreted to the base of the orogenic wedge at this time, displacing the Temsamane rocks upwards, which then underwent strain localization of the simple shear into both the extensional and compressional shear zones systems.

7.4. Tectonic model for the evolution of the Eastern Rif

Numerous geodynamic models have been proposed for the evolution of the Betic–Rif orogeny, and those models include: subduction roll-back, slab break-off, or lithospheric delamination (see Platt et al., 2013, for review). All the previous models include the advance of the continental crust of the Alborán Domain towards the west between the European and African plates (e.g., Balanyá et al., 2007; Booth-Rea et al., 2005; Chalouan et al., 2008; Platt et al., 2003, 2013), which, in turn, implied an oblique collision in the southern branch of the Betic–Rif orogen, generating a left-lateral transpressional regime affecting the North African paleomargin. For example, models that include roll-back of the subduction towards the NW of the Mesozoic oceanic crust of the Tethys below the European crust from 30 to 10 Ma (e.g., Faccenna et al., 2004; Rosenbaum and Lister, 2004; Rosenbaum et al., 2002) produced the generation of the actual oceanic crust of the Western Mediterranean Sea. Furthermore, it also produced the migration of a group of terranes that collided with Apulia, Northwest Africa and Southeastern Iberia to produce the Apenines, Peloritan–Calabrian arc, Tell and Betic–Rif chains (e.g., Faccenna et al., 2004; Rosenbaum and Lister, 2004; Rosenbaum et al., 2002).

The architecture of the eastern Rif indicates that both basement and cover of the North African paleomargin (Temsamane fold-and-thrust stack) were accreted into the southern branch of the orogen and thrust over by the Tanger–Ketama + Aknoul units, which in turn were thrust over by the Maghrebian Flyschs and the Alborán Domain (see Figs. 1, 2, and 15) to produce an orogenic wedge (Chalouan and Michard, 2004; Chalouan et al., 2008). The main trace of the suture of the Tethys Ocean is defined by the trace of the base of the Maghrebian Flysch units (Duran-Delga et al., 2000) and has roughly NE–SW strikes and NW dips (Figs. 1, 2, and 15). Our data indicate that the Rifean orogenic wedge was already formed at 21 Ma showing that the Alborán domain have collided with the Northwestern African paleomargin at this time during its movement towards the west.

The D_p deformational event most likely recorded the moment when the paleomargin rocks of the Temsamane units were thrust over and

their northern rocks reached intermediate crustal conditions below the orogenic wedge with low geothermal gradients, whereas the southern extreme rocks were at late diagenetic conditions (around 230 °C). The kinematic indicators such as S-C, S-C′ structures, and σ and δ porphyroclasts indicate a general top-to-the-WSW sense of shear (Fig. 6C and D). These data suggest that the Temsamane rocks were in an inclined transpressional zone in the sense of Jones et al. (2004). The ^{40}Ar/^{39}Ar radiometric ages on white mica and amphibole crystals indicates that the transpressional orogenic wedge was built at Aquitanian times, and probably it was formed at earlier times during the Oligocene.

The radiometric ages from ~21 to ~15 Ma determined in this work for the D_p metamorphic event indicates that Temsamane rocks maintained at almost the same temperature during 6 Ma. These data can be explained if the transpressional orogenic wedge was stable from Aquitanian to Langhian times, and the Temsamane rocks remained at the base of the wedge without significant vertical movements and cooling stages.

Distributions of orientations of stretching lineations with a large range of lineation orientations that can spread along complete girdles are predicted in most of the models of transpressional shear zones and also are recorded in the data from natural transpressional shear zones (e.g., Fernández and Díaz-Azpiroz, 2009, and references therein).

The D_c deformational event recorded the vertical uplift within the transpressional orogenic wedge of the Temsamane rocks and therefore most probably resulted from the evolution of D_p transpressional regime trough time. According the previously discussed radiometric data, the most likely age for the D_c event was between Langhian and Early Tortonian times.

During the D_c deformational event, the simple shear component of the transpression was localized in two different set of structures with the same kinematic but opposite effects: below, in the imbricated shear zones acting as left-lateral strike–slip reverse faults producing thickening of the Temsamane stack, and upwards in the extensional detachment producing the thinning of the Tanger–Ketama and Aknoul units. Fragments of the Jurassic sequence of the Tanger–Ketama unit and of the uppermost Temsamane units remained as extensional duplex within the extensional detachment system.

Both set of compressional and extensional structures have the same WSW–ENE trend for the stretching lineation (with a mean N80°E trend). Furthermore, the coaxial component recorded by the F_c trend of folds remains non-localized in the entire deformational zone, and the low dipping F_c axial surfaces indicate that they accommodate a roughly sub-vertical shortening. This localization of the shear strain was predicted by Lin et al. (1998, 1999) and Jiang et al. (2001) for transpressional shear zones as a material necessity.

8. Conclusions

The structure of the Temsamane fold-and-thrust stack corresponds to four tectonic units limited by anastomosing ductile shear zones cutting a trend of south-vergent recumbent folds. The ductile fold-and-thrust stack was formed in an inclined left-handed transpressional zone during the Chattian to Langhian, producing two main deformational events. The first deformational event (D_p) produced a planar linear fabric (S_p/L_p) in a non-coaxial regime with a top-to-the-WSW sense of movement and was associated to P–T conditions ranging from late diagenesis in the southernmost Temsamane outcrops to epizone in the north. According to the ^{40}Ar/^{39}Ar ages, this deformation occurred at Chattian–Aquitanian times.

The second deformational event (D_c event) occurred at around 15 Ma (Langhian) and generated ENE–WSW trending folds with SSE vergence and a set of anastomosing shear zones with a planar linear fabric (S_m/L_m). The shear zones have a hinterland-dipping duplex geometry with a roof shear zone at the base of the uppermost Ras Afraou unit. Similarities in the orientations, and shear regimes between both

deformational events (D_p and D_c) suggest that they can be the result of a unique deformational regime, where D_c was the evolution in time from D_p event. Concretely, the imbricated shear zones may account for localization of the shear strain into narrow bands cutting the lithological sequence.

Formation of the F_c recumbent fold-nappes cut by shear zones with a stretching lineation sub-parallel to the fold hinges can be explained by a mechanism combining a deformation in a regime of simple shear, and a superposed coaxial strain with sub-vertical maximum shortening. The latter can account for the sub-horizontal S_{c+1} foliations and the kinematics of the Temsamane detachment, which in turn can explain most of the uplift of the Temsamane rocks from the middle to the uppermost crust.

The described evolution indicates that the formation of the Rifean orogenic wedge produced by the collision between the western Mediterranean terranes and the North African paleomargin occurred at Chattian to Langhian times. The orogenic wedge most likely was stable from Aquitanian to Langhian times, and the Temsamane rocks remained at the base of the wedge without significant vertical movements and cooling stages, when movement along the Temsamane detachment recorded the uplift of the Temsamane rocks from the middle to the uppermost crust produced by the destabilization of the wedge.

Acknowledgments

References

Andrieux, J., 1971. La structure du Rif central. Notes du Service Géologique du Maroc (235 pp., Rabat, Morocco).
Asebriy, L., 1994. Evolution tectonique et métamorphique du Rif central (Maroc): définition du domaine Subrifain. (Ph.D. thesis), University of Rabat, Rabat, Morocco (248 pp.).
Asebriy, L., de Luca, P., Bourgois, J., Chotin, P., 1987. Resédimentation d'âge sénonien dans le Rif central (Maroc): conséquences sur les divisions paléogéographiques et structurales de la chaîne. J. Afr. Earth Sci. 6, 9–17.
Asebriy, L., Azdimousa, A., Bourgois, J., 2003. Structure du Rif externe sur la transversale du Massif de Ketama. Trav. Inst. Sci. Rabat, Maroc 21, 27–46.
Azdimousa, A., Bourgois, J., Poupeau, G., Montigny, R., 1998. Histoire thermique du massif de Kétama (Maroc); sa place en Afrique du Nord et dans les Cordillères Bétiques. C. R. Acad. Sci. Paris 326, 847–853.
Azdimousa, A., Bourgois, J., Asebriy, L., Poupeau, G., Montigny, R., 2003. Histoire thermique et surrection du Rif externe et des nappes de flyschs associées (Nord Maroc). Trav. Inst. Sci. Rabat 21, 15–26.
Azdimousa, A., Poupeau, G., Rezqui, H., Asebriy, L., Bourgois, J., Aït Brahim, L., 2006. Géodynamique des bordures méridionales de la mer d'Alboran; application de la stratigraphie séquentielle dans le bassin néogène de Boudinar (Rif oriental, Maroc). Bull. Inst. Sci. Rabat Sci. Terre 28, 9–18.
Azdimousa, A., Jabaloy, A., Asebriy, L., Booth-Rea, G., González-Lodeiro, F., Bourgois, J., 2007. Lithostratigraphy and structure of the Temsamane unit (eastern external Rif, Morocco). Rev. Soc. Geol. Esp. 20, 187–200.
Balanyá, J.C., García-Dueñas, V., 1987. Les directions structurales dans le Domaine d'Alborán de part et d'autre du D'etroit de Gibraltar. C. R. Acad. Sci. 304, 929–932.
Balanyá, J.C., Crespo-Blanc, A., Azpiroz, M.D., Exposito, I., Lujan, M., 2007. Structural trend line pattern and strain partitioning around the Gibraltar Arc accretionary wedge: insights as to the mode of orogenic arc building. Tectonics 26. http://dx.doi.org/10.1029/2005tc001932.

Bastida, F., Aller, J., Fernández, F.J., Lisle, R.J., Bobillo-Ares, N.C., Menéndez, O., 2014. Recumbent folds: key structural elements in orogenic belts. Earth Sci. Rev. 135, 162–183. http://dx.doi.org/10.1016/j.earscirev.2014.05.002.
Behr, W.M., Platt, J.P., 2012. Kinematic and thermal evolution during two-stage exhumation of a Mediterranean subduction complex. Tectonics 31, TC4025.
Benzaggagh, M., 2015. Basaltos toleíticos, complejos ofiolíticos del límite Jurásico-Cretácico del Mesorif (Rif externo, Marruecos) y la importancia del accidente del Ouerrha en la evolución paleogeográfica y geodinámica del Rif externo. Bol. Geol. Min. (in press).
Benzaggagh, M., Mokhtari, A., Rossi, P., Michard, A., El Maz, A., Chalouan, A., Saddiqi, O., Rjimati, E., 2013. Oceanic units in the core of the External Rif (Morocco): intramargin hiatus or South-Tethyan remnants? Journal of Geodynamics 77, 4–21.
Benzaggagh, M., Mokhtari, A., Rossi, P., Michard, A., El Maz, A., Chalouan, A., Saddiqi, O., Rjimati, E.-C., 2014. Oceanic units in the core of the External Rif (Morocco): intramargin hiatus or South-Tethyan remnants? J. Geodyn. 77, 4–21. http://dx.doi.org/10.1016/j.jog.2013.10.003.
Booth-Rea, G., Azañón, J.M., Martínez-Martínez, J.M., Vidal, O., García-Dueñas, V., 2005. Contrasting structural and P–T evolutions of tectonic units in the southeastern Betics: key for understanding the exhumation of the Alboran Domain HP/LT crustal rocks (Western Mediterranean). Tectonics 24. http://dx.doi.org/10.1029/2004TC001640.
Booth-Rea, G., Jabaloy-Sánchez, A., Azdimousa, A., Asebriy, L., Vázquez-Vílchez, M., Martínez-Martínez, J.M., 2012. Upper-crustal extension during oblique collision: the Temsamane extensional detachment (eastern Rif, Morocco). Terra Nova 24, 505–512. http://dx.doi.org/10.1111/j.1365-3121.2012.01089.x.
Bourgois, J., 1977. D'une étape géodynamique majeure dans la genèse de l'arc de Gibraltar: "L'hispanisation des flyschs rifains au Miocène inférieur". Bull. Soc. Geol. Fr. XIX, 115–1119.
Chalouan, A., Michard, A., 2004. The Alpine Rif belt (Morocco): a case of mountain building in a subduction-subduction-transform fault triple junction. Pure Appl. Geophys. 161 (3), 489–519.
Chalouan, A., Michard, A., El Kadiri, K., Negro, F., Frizon de Lamotte, D., Soto, J.I., Saddiqi, O., 2008. The Rif Belt. In: Michard, A., Frizon de Lamotte, D., Saddiqi, O., Chalouan, A. (Eds.), Continental Evolution: The Geology of Morocco, Lecture Notes in Earth Sciences. vol. 116. Springer-Verlag, Berlin Heidelberg, pp. 203–302.
Choubert, G., A. Faure-Muret, E. A. Hilali, J. P. Houzay, and D. Frizon de Lamotte, (1984), Carte géologique du Rif, échelle 1/50000, feuille Boudinar, Notes et Mémoires du Service Géologique du Maroc, 299.
Czeck, D.M., Hudleston, P.J., 2003. Testing models for obliquely plunging lineations in transpression: a natural example and theoretical discussion. J. Struct. Geol. 25, 959–982.
Dewey, J.F., Holdsworth, R.E., Strachan, R.A., 1998. Transpression and transtension zones. In: Holdsworth, R.E., Strachan, R.A., Dewey, J.F. (Eds.), Continental Transpression and Transtension Tectonics. Geological Society, London, Special Publication vol. 135, pp. 1–14 (London, United Kingdom).
Díaz Azpiroz, M., Fernández, C., 2005. Kinematic analysis of the southern Iberian shear zone and tectonic evolution of the Acebuches metabasites (SW Variscan Iberian Massif). Tectonics 24. http://dx.doi.org/10.1029/2004TC001682.
Do Campo, M., Nieto, F., 2003. Transmission electron microscopy study of the very low-grade metamorphic evolution in Neoproterozoic Pelites of the Puncoviscana Formation (Cordillera Oriental, NWArgentina). Clay Minerals 38, 459–481.
Duggen, S., Hoernle, K., van den Bogaard, P., Harris, C., 2004. Magmatic evolution of the Alboran region: the role of subduction in forming the western Mediterranean and causing the Messinian Salinity Crisis. Earth Planet. Sci. Lett. 218, 91–108. http://dx.doi.org/10.1016/S0012-821X(03)00632-0.
Duggen, S., Hoernle, K., Van den Bogaard, P., Garbe-Schonberg, D., 2005. Post-collisional transition from subduction- to intraplate-type magmatism in the Westernmost Mediterranean: evidence for continental-edge delamination of subcontinental lithosphere. J. Petrol. 46, 1155–1201.
Durand-Delga, M., Hottinger, L., Marcais, J., Mattauer, M., Milliard, Y., Suter, G., 1962. Données actuelles sur la structure du Rif. Livre à la mémoire du professeur Fallot. Soc. Géol. Fr. Mém. 1, 399–442 (Paris).
Duran-Delga, M., Rossi, P., Olivier, P., Puglisi, D., 2000. Situation structurale et nature ophiolitique de roches basiques jurassiques associées aux flyschs maghrébins du Rif (Maroc) et de Sicile (Italie). C. R. Acad. Sci. Paris II 331 (1), 29–38.
Dutton, B.J., 1997. Finite strains in transpression zones with no boundary slip. J. Struct. Geol. 19, 1189–1200.
Elazzab, D., Galdeano, A., Feinberg, H., Michard, A., 1997. Prolongement en profondeur d'une écaille ultrabasique allochtone: traitement des données aéromagnétiques et modélisation 3D des péridotites des Beni Malek (Rif, Maroc). Bull. Soc. Geol. Fr. 168, 667–683.
Faccenna, C., Piromallo, C., Crespo-Blanc, A., Jolivet, L., Rossetti, F., 2004. Lateral slab deformation and the origin of the western Mediterranean arcs. Tectonics 23, TC1012.
Fernández, C., Díaz-Azpiroz, M., 2009. Triclinic transpression zones with inclined extrusion. J. Struct. Geol. 31, 1255–1269.
Fossen, H., 2010. Structural Geology. Cambridge University Press, Cambridge (463 pp).
Frizon de Lamotte, D., 1985. La structure du Rif oriental (Maroc). Rôle de la tectonique longitudinale et importance des fluides. (Ph. D. thesis), University Paul et Marie Curie, Paris VI, France (436 pp.).
Frizon de Lamotte, D., 1987. Un exemple de collage synmétamorphe: la déformation miocène des Temsamane (Rif externe, Maroc). Bull. Soc. Geol. Fr. 3, 337–344.
Gil, A., Gallart, J., Diaz, J., Carbonell, R., Torne, M., Levander, A., Harnafi, M., 2014. Crustal structure beneath the Rif Cordillera, North Morocco, from the RIFSIS wide-angle reflection seismic experiment, Geochemistry, Geophysics. Geosystems 15, 4712–4733.
Gómez-Pugnaire, M.T., Rubatto, D., Fernández-Soler, J.M., Jabaloy, A., López Sánchez-Vizcaíno, V., González-Lodeiro, F., Galindo-Zaldívar, J., Padrón-Navarta, J.A., 2012. U-Pb geochronology of Nevado-Filábride gneisses: evidence for the Variscan nature of

the deepest Betic complex (SE Spain). Lithos 146–147, 93–111. http://dx.doi.org/10.1016/j.lithos.2012.03.027.

Guidotti, C.V., Sassi, F.P., 1986. Classification and correlation of metamorphic facies series by means of muscovite b$_0$ data from low-grade metapelites. Neues Jb. Mineral. Abh. 153, 363–380.

Harland, W.B., 1971. Tectonic transpression in Caledonian Spitsbergen. Geol. Mag. 108, 27–49.

Harrison, T.M., 1981. Diffusion of ^{40}Ar in hornblende. Contrib. Mineral. Petrol. 78, 324–331.

Harrison, T.M., Célérier, J., Aikman, A.B., Hermann, J., Heizler, M.T., 2009. Diffusion of ^{40}Ar in muscovite. Geochim. Cosmochim. Acta 73, 1039–1051. http://dx.doi.org/10.1016/j.gca.2008.09.038.

Jiang, D., 2007. Sustainable transpression: an examination of strain and kinematics in deforming zones with migrating boundaries. J. Struct. Geol. 29, 1984–2005.

Jiang, D., Lin, S., Williams, P.F., 2001. Deformation paths in high-strain zones, with reference to slip partitioning in transpressional plate-boundary regions. J. Struct. Geol. 23, 991–1005.

Jolivet, L., Faccenna, C., Goffé, B., Burov, E., Agard, P., 2003. Subduction tectonics and exhumation of high-pressure metamorphic rocks in the Mediterranean orogens. Am. J. Sci. 303, 353–409.

Jones, R.R., Holdsworth, R.E., Clegg, P., McCaffrey, K., Tavarnelli, E., 2004. Inclined transpression. J. Struct. Geol. 26, 1531–1548.

Kisch, H.J., 1991. Illite 'crystallinity': recommendations on sample preparation, X-ray diffraction settings and interlaboratory samples. J. Metamorph. Geol. 9, 665–670.

Kisch, H.J., Árkai, P., Brime, C., 2004. On the calibration of the Illite Kübler Index (Illite "crystallinity"). Schweiz. Mineral. Petrogr. Mitt. 84, 323–331.

Kretz, R., 1983. Symbols of rock-forming minerals. American Mineralogist 68, 277–279.

Leake, B.E., Woolley, A.R., Arps, C.E.S., Birch, W.D., Gilbert, M.C., Grice, J.D., Hawthorne, F.C., Kato, A., Kisch, H.J., Krivovichev, V.G., Linthout, K., Laird, J., Mandarino, J.A., Maresch, W.V., Nickel, E.H., Rock, N.M.S., Schumacher, J.C., Smith, D.C., Stephenson, N.C.N., Ungaretti, L., Whittaker, E.J.W., Youzhi, G., 1997. Nomenclature of amphiboles: report of the Subcommittee on Amphiboles of the International Mineralogical Association, Commission on New Minerals and Mineral Names. Mineral. Mag. 61, 295–321.

Leblanc, D., 1975–1979. Etude géologique du Rif externe oriental au Nord de Taza (Maroc). Notes et Mémoires du Service Géologique du Marocp. 281.

Leikine, M., Asebriy, L., Bourgois, J., 1991. Sur l'âge du métamorphisme anchiépizonal de l'únité de Ketama, Rif central (Maroc). C. R. Acad. Sci. Paris 313, 787–793.

Lin, S., Jiang, D., Williams, P.F., 1998. Transpression (or transtension) zones of triclinic symmetry: natural example and theoretical modeling. In: Holdsworth, R.E., Strachan, R.A., Dewey, J.F. (Eds.), Continental Transpression and Transtension Tectonics. Geological Society, London, Special Publication vol. 135, pp. 41–57.

Lin, S., Jiang, D., Williams, P.F., 1999. Discussion on transpression and transtension zones. J. Geol. Soc. Lond. 156, 1045–1048.

Mancilla, F. de L., Stich, D., Morales, J., Julià, J., Diaz, J., Pazos, A., Córdoba, D., Pulgar, J.A., Ibarra, P., Harnafi, M., Gonzalez-Lodeiro, F., 2012. Crustal thickness variations in northern Morocco. J. Geophys. Res. 117, B02312. http://dx.doi.org/10.1029/2011JB008608.

McDougall, I., Harrison, T.M., 1999. Geochronology and Thermochronology by the ^{40}Ar/^{39}Ar Method. Oxford University Press, New York (269 pp).

Merriman, R.J., 2005. Clay minerals and sedimentary basin history. Eur. J. Mineral. 17, 7–20.

Merriman, R.J., Frey, M., 1999. Patterns of Very Low-Grade Metamorphism in Metapelitic Rocks. In: Frey, M., Robinson, D. (Eds.), Low-Grade Metamorphism. Blackwell Science, Oxford, pp. 61–107.

Merriman, R.J., Peacor, D.R., 1999. Very low-grade metapelites: mineralogy, microfabrics and measuring reaction progress. In: Frey, M., Robinson, D. (Eds.), Low-Grade metamorphism. Blackwell Science, Oxford, pp. 10–60.

Michard, A., Feinberg, H., El-Azzab, D., Bouybaouène, M., Saddiqi, O., 1992. A Serpentinite ridge in a collisional paleomargin setting: the Beni Malek Massif, external Rif, Morocco. Earth Planet. Sci. Lett. 113 (3), 425–442.

Michard, A., Frizon de Lamotte, D., Negro, F., Saddiqi, O., 2007. Serpentinite slivers and metamorphism in the External Maghrebides: arguments for an intracontinental suture in the African paleomargin (Morocco, Algeria). Rev. Soc. Geol. Esp. 20, 173–185.

Michard, A., Chalouan, A., Negro, F., Saddiqi, O., 2015. Comment on "Evidence of extensional metamorphism associated to Cretaceous rifting of the North-Maghrebian passive margin: the Tanger–Ketama Unit (External Rif, Northern Morocco)" by Vázquez et al., Geologica Acta, 11 (2013), 277-293. Geol. Acta (in press).

Molnar, P., 1992. Brace–Goetze strength profiles, the partitioning of strike slip and thrust faulting at zones of oblique convergence, and the stress shear flow paradox of the San Andreas Fault. In: Evans, B., Wong, T.-F. (Eds.), Fault Mechanics and Transport Properties of Rocks. Academic Press, London, pp. 435–459.

Monie, P., Frizon de Lamotte, D., Leikine, M., 1984. Etude géochronologique préliminaire par la méthode ^{39}Ar/^{40}Ar du métamorphisme alpin dans le rif externe (Maroc); précisions sur le calendrier tectonique tertiaire. Rev. Géol. Dynam. Géog. Phys. 25 (4), 307–317.

Negro, F., 2005. Exhumation des roches métamorphiques du domaine d´Alboran: étude de la Chaine Rifaine (Maroc) et corrélation avec les Cordillères Bétiques (Espagne). (Ph. D. Thesis), University of Paris XI (99 pp.).

Negro, F., Agard, P., Goffé, B., Saddiqi, O., 2007. Tectonic and metamorphic evolution of the Temsamane units, External Rif (northern Morocco): implications for the evolution of the Rif and the Betic–Rif arc. J. Geol. Soc. Lond. 164, 829–842.

Negro, F., de Sigoyer, J., Goffé, B., Saddiqi, O., Villa, I.M., 2008. Tectonic evolution of the Betic–Rif arc: new constraints from ^{40}Ar/^{39}Ar dating on white micas in the Temsamane units (External Rif, northern Morocco). Lithos 106, 93–108. http://dx.doi.org/10.1016/j.lithos.2008.06.011.

Nieto, F., Mata, P., Bauluz, B., Giorgetti, G., Árkai, P., Peacor, D.R., 2005. Retrograde diagenesis, a wide spread process on a regional scale. Clay Miner. 40, 93–104.

Platt, J.P., 1993. Mechanics of oblique convergence. J. Geophys. Res. 98, 16239–16256.

Platt, J.P., Allerton, S., Kirker, A., Mandeville, C., Mayfield, A., Platzman, E.S., Rimi, A., 2003. The ultimate arc: differential displacement, oroclinal bending, and vertical axis rotation in the External Betic–Rif arc. Tectonics 22. http://dx.doi.org/10.1029/2001TC001321.

Platt, J.P., Behr, W.M., Johanesen, K., Williams, J.R., 2013. The Betic–Rif arc and its orogenic hinterland: a review. Ann. Rev. Earth Planet. Sci. 41, 14.1–14.45. http://dx.doi.org/10.1146/annurev-earth-050212-123951.

Potel, S., Ferreiro Mählmann, R., Stern, W.B., Mullis, J., Frey, M., 2006. Very low-grade metamorphic evolution of pelitic rocks under high-pressure/low-temperature conditions, NW New Caledonia (SW Pacific). J. Petrol. 47 (5), 991–1015. http://dx.doi.org/10.1093/petrology/egl001.

Ramsay, J.G., 1967. Folding and Fracturing of Rocks. McGraw-Hill, New York (568 pp).

Ramsay, J.G., Casey, M., Kligfield, R., 1983. Role of shear in development of the Helvetic fold-thrust belt of Switzerland. Geology 11, 439–442.

Renne, P.R., Swisher, C.C., Deino, A.L., Karner, D.B., Owens, T.L., DePaolo, D.J., 1998. Intercalibration of standards, absolute ages and uncertainties in ^{40}Ar/^{39}Ar dating. Chem. Geol. 145, 117–152.

Rosenbaum, G., Lister, G.S., 2004. Formation of arcuate orogenic belts in the western Mediterranean region. Geol. Soc. Am. Spec. Pap. 383, 41–56.

Rosenbaum, G., Lister, G.S., Duboz, C., 2002. Relative motions of Africa, Iberia and Europe during Alpine orogeny. Tectonophysics 359, 117–129.

Rossetti, F., Theye, T., Lucci, F., Bouybaouene, M.L., Dini, A., Gerdes, A., Phillips, D., Cozzupoli, D., 2010. Timing and modes of granite magmatism in the core of the Alboran Domain, Rif chain, northern Morocco: implications for the Alpine evolution of the western Mediterranean. Tectonics 29. http://dx.doi.org/10.1029/2009TC002487.

Sanderson, D.J., Marchini, W.R.D., 1984. Transpression. J. Struct. Geol. 6, 449–458.

Sarkarinejad, K., Azizi, A., 2008. Slip partitioning and inclined dextral transpression along the Zagros Thrust System, Iran. J. Struct. Geol. 30, 116–136.

Schiffman, P., Fridleifsson, G.O., 1991. The smectite–chlorite transition in drillhole NJ-15, Nesjavellir geothermal field, Iceland: XRD, BSE and electron microprobe investigations. J. Metamorph. Geol. 9, 679–696.

Spotila, J.A., Niemi, N., Brady, R., House, M., Buscher, J., Oskin, M., 2007. Long-term continental deformation associated with transpressive plate motion: the San Andreas fault. Geology 35, 967–970. http://dx.doi.org/10.1130/G23816A.

Stone, P., Merriman, R.J., 2004. Basin thermal history favours an accretionary origin for the Southern Uplands terrane, Scottish Caledonides. J. Geol. Soc. Lond. 161, 829–836.

Suter, G., (1980), Carte structurale de la chaîne rifaine à 1/500000. Notes et Mémoires du Service Géologique, Maroc.

Vázquez, M., Asebriy, L., Azdimousa, A., Jabaloy, A., Booth-Rea, G., Barbero, L., Mellini, M., González-Lodeiro, F., 2013. Evidence of extensional metamorphism associated to Cretaceous rifting of the North-Maghrebian passive margin: the Tanger–Ketama unit (External Rif, northern Morocco). Geol. Acta 11, 277–293.

Vázquez, M., Asebriy, L., Azdimousa, A., Jabaloy, A., Booth-Rea, G., Barbero, L., Mellini, M., González-Lodeiro, F., 2013. Reply to the comment by Michard et al. on "Evidence of extensional metamorphism associated to Cretaceous rifting of the North-Maghrebian passive margin: The Tanger–Ketama Unit (External Rif, Northern Morocco) by Vázquez et al., Geologica Acta 11 (2013), 277–293". Geol. Acta. (in press).

Vidal, J.F., 1971. Une interprétation nouvelle des nappes du Prérif central (Maroc) et ses conséquences sur la structure de leur substratum autochtone. C. R. Acad. Sci. Paris D 272, 24–27.

Villa, I.M., Ruggieri, G., Puxeddu, M., 1997. Petrological and geochronological discrimination of two white-mica generations in a granite cored from the Larderello–Travale geothermal field (Italy). Eur. J. Mineral. 9, 563–568.

Vollmer, F.W., 1990. An application of eigenvalue methods to structural domain analysis. Geol. Soc. Am. Bull. 102, 786–791.

Warr, L.N., Rice, A.H.N., 1994. Interlaboratory standardization and calibration of clay mineral crystallinity and crystallite size data. J. Metamorph. Geol. 12, 141–152.

Whitney, D.L., Evans, B.W., 2010. Abbreviations for names of rock-forming minerals. Am. Mineral. 95, 185–187.

Woodcock, N.H., 1977. Specification of fabric shapes using an eigenvalue method. Geol. Soc. Am. Bull. 88, 1231–1236.